JM PAPERS

Prediction of the droplet size distribution in aerodynamic droplet breakup

Isaac M. Jackiw[1] and Nasser Ashgriz[1],†

[1]Department of Mechanical and Industrial Engineering, University of Toronto, Toronto, ON M5S 3G8, Canada

The rim and bag dynamics in aerodynamic droplet breakup are investigated experimentally and theoretically. Three main modes contribute to the breakup sizes in aerodynamic droplet breakup: the rim node, the remaining rim and the bag breakup modes. However, existing models only consider one mode and are, therefore, unable to predict the size distribution. The present theoretical work seeks to model the dominant breakup mechanisms of each mode and to relate these mechanisms to the size distribution. It is shown that the nodes can be modelled using either the Rayleigh–Taylor or Rayleigh–Plateau instabilities with comparable results and that the variation in the node sizes results from the variation in the amount of mass in the rim that flows into the node prior to the rim breakup. The breakup of the rim is shown to be a result of a combination of the Rayleigh–Plateau instability and a newly proposed collision mechanism, wherein the impact of the corrugated receding rim of the bag with the main rim forces the main rim to break with the same wavelength as the receding rim. The resulting size distribution of the droplet breakup is estimated assuming that the relative weighting of the breakup mechanisms for each mode follows a two-parameter gamma distribution. The volume of each geometry is used to estimate the volume weighting of the modes, giving a reasonable prediction of the size distribution resulting from aerodynamic droplet breakup.

Key words: aerosols/atomization, drops, breakup/coalescence

1. Introduction

The breakup of liquid droplets due to aerodynamic forces is a canonical problem in fluid dynamics and is one of the most fundamental aspects of spray atomization. In a wide range of applications including but not limited to combustion, surface coating, pharmaceutical manufacturing and disease transmission modelling, the most important result of droplet breakup is the distribution of the child droplet sizes. Although aerodynamic droplet

† Email address for correspondence: ashgriz@mie.utoronto.ca

breakup has been studied extensively for decades, a consensus has not been reached as to the underlying mechanisms of breakup that lead to the distribution in child droplet sizes.

The aerodynamic breakup of liquid droplets can be parametrized by the Weber number and the Ohnesorge number (Pilch & Erdman 1987) given by

$$We = \frac{\rho_g U^2 d_0}{\sigma} \qquad (1.1)$$

and

$$Oh = \frac{\mu_l}{\sqrt{\rho_l \sigma d_0}}, \qquad (1.2)$$

where ρ_g and ρ_l are the gas- and liquid-phase densities in kg m^{-3}, μ is the liquid viscosity in Pa s, σ is the interfacial surface tension in N m^{-1}, d_0 is the initial diameter of the droplet in m and U is the relative velocity between the gas and the droplet in m s^{-1}. When analysing the transient aspects of droplet breakup, a dimensionless time, T (equation (1.3)), which is non-dimensionalized by a characteristic deformation time, τ (equation (1.4)), is conventionally used to scale time:

$$T = \frac{t}{\tau}, \qquad (1.3)$$

$$\tau = \frac{d_0}{U} \sqrt{\frac{\rho_l}{\rho_g}}. \qquad (1.4)$$

The characteristic deformation time naturally arises in the non-dimensionalization of several droplet-breakup analyses such as the displacement of a droplet undergoing constant acceleration (Ranger & Nicolls 1969), instability theories (Pilch & Erdman 1987) or the oscillation of a drop under aerodynamic loading (Rimbert *et al.* 2020), the latter being the appropriate case for the present work.

Aerodynamic droplet breakup is a transient process and is typically divided into two stages: initiation and breakup (Pilch & Erdman 1987). Images showing the deformation and breakup of a droplet are presented in figure 1(*a*). In the initiation phase, the initially spherical droplet is deformed by the airflow until its frontal surface becomes a flat disk, termed the windward disk, while the rearward portion of the droplet can remain as an undeformed core (Jackiw & Ashgriz 2021). The periphery of the windward disk forms a rim that surrounds the droplet. In the breakup phase, the interior portion of the windward disk is blown out into a thin bag, which then ruptures, leading to the breakup of the bag and ultimately the rim. If the undeformed core is sufficiently small, it may deform with the bag. A larger undeformed core may form a stamen at the centre of the bag that persists throughout the breakup, or may remain after the breakup of the bag and rim to undergo further breakup by the same process.

The undeformed core defines the morphology of the breakup. When there is little to no undeformed core, the breakup morphology is 'bag' breakup. If the undeformed core is significant but does not undergo further breakup, (i.e. it forms a stamen) then the morphology is 'bag and stamen' (BS) (see figure 1*b*). If the undeformed core is large enough to undergo further breakup, then the morphology is termed 'multibag' (MB) if several bags form azimuthally about the core (see figure 1*c*), or sheet-thinning (ST) if the rim is drawn downstream around the core by the surrounding airflow (see figure 1*d*). If the entire droplet breaks up instantaneously, then the morphology of the breakup is 'catastrophic'. For a review of the models and theories developed for the initiation phase,
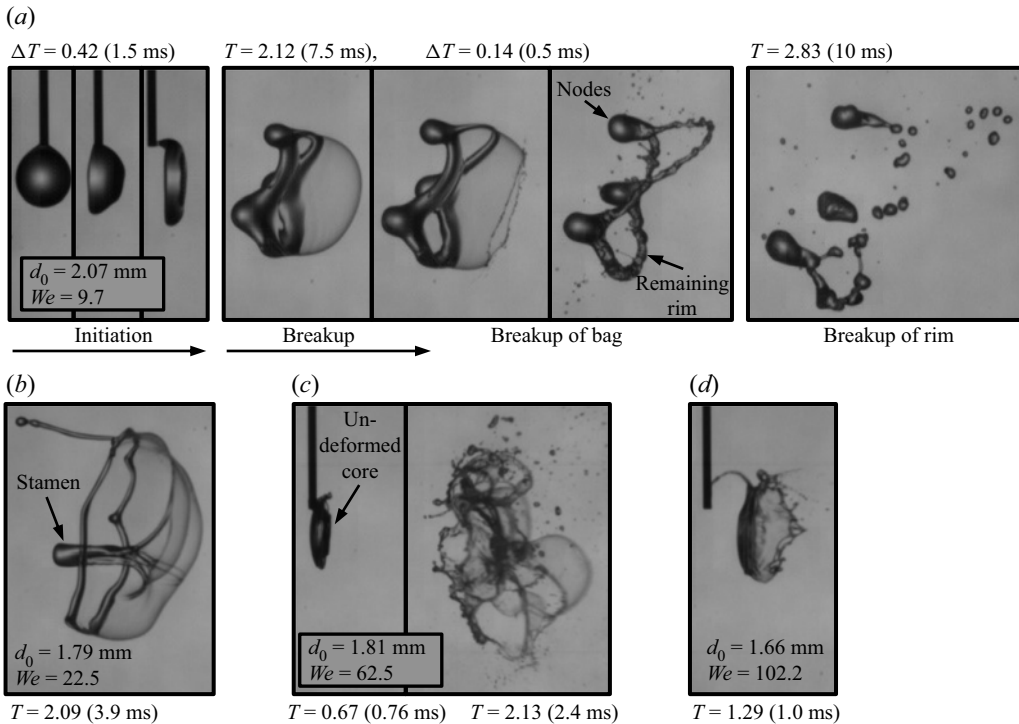
Figure 1. Images showing (*a*) the deformation and bag breakup of a droplet (see supplementary movie 1 available at https://doi.org/10.1017/jfm.2022.249), (*b*) BS breakup, (*c*) the formation of the undeformed core and subsequent MB breakup and (*d*) ST breakup.

see Jackiw & Ashgriz (2021). Many works have studied the dynamic deformation that is undergone throughout the initiation and breakup phases; however, few ultimately develop an understanding of the child droplet sizes that result from the breakup and those that do typically only predict a single characteristic size and not the distribution of sizes.

Although numerical simulations provide a powerful tool for analysing droplet breakup, much work is still needed to improve their agreement with experiments (Strotos *et al.* 2016; Xiao, Dianat & McGuirk 2016). One of the main limitations of numerical simulations of aerodynamic droplet breakup is mesh-induced breakup, wherein the mesh size is not fine enough to resolve microscale phenomena, such as the dynamics in the breakup of the bag. This impedes even qualitative agreement between simulations and experiments near the breakup point (Strotos *et al.* 2016). Nevertheless, numerical simulations have been useful in revealing the physical trends in droplet deformation at low density ratios (i.e. where the gas- and liquid-phase densities are close), where the computational costs are not as high (Han & Tryggvason 2001; Jain *et al.* 2019; Marcotte & Zaleski 2019). A comparison of the work of Marcotte & Zaleski (2019) with our earlier work is presented in Appendix A; however, such ranges of density ratio are not in the scope of the present work. Numerical simulations have also been used to study the mechanisms of liquid jet breakup, where features similar to those of droplet breakup, such as rims and bags, have been revealed to play a role in jet atomization (Behzad, Ashgriz & Karney 2016). While the capabilities of the numerical simulation of aerodynamic droplet breakup are constantly improving, analytical models remain highly relevant as they provide a clearer insight into the important underlying physical phenomena dominating the breakup.

Furthermore, analytical models are significantly less computationally intense, making them better suited for use in spray modelling where many thousands of droplets must be analysed.

Many works concerning aerodynamic droplet breakup modelling consider single mechanisms that break the droplet immediately after the initiation deformation. Mass–spring–damper models, such as the Taylor analogy breakup model (O'Rourke & Amsden 1987), typically consider a critical criterion for breakup at which point the child droplet sizes are determined. For example, in the classical Taylor analogy breakup model, the oscillatory energy of a droplet at a critical deformation is compared with the surface energy of the equally sized child droplets that result from the breakup to determine their number and size. The child droplets are then analysed considering their new size and speed to determine if further breakup occurs. By assuming this breakup cascade, a size distribution may be reached for a spray; however, for the breakup of an individual droplet, the child droplet sizes are still monodispersed. Although such models are used widely in industrial fluid dynamics software for low-*We* breakup (ANSYS Inc 2011), they neither mechanistically describe the complex breakup processes nor predict the child droplet size distribution that results from the aerodynamic breakup of a single droplet.

Some models have proposed a mechanistic view of the breakup where it is assumed that surface instabilities play a major role in the atomization of droplets, particularly at high *We*. The 'Rayleigh–Taylor piercing' mechanism describes the rapid breakup of a flattened droplet by the penetration of surface waves generated on the windward face of the droplet due to rapid acceleration (Joseph, Beavers & Funada 2002; Theofanous & Li 2008; Sharma *et al.* 2021). The Rayleigh–Taylor piercing mechanism has also been used to describe the breakup at low *We*, where it has been claimed to be the cause of the bag formation; however, recent works have called this into question, showing that the deformation rate is more strongly correlated to the breakup morphology and sizes at low *We* (Jackiw & Ashgriz 2021). At even higher *We*, the 'shear-induced entrainment' mechanism describes the shearing of waves from the periphery of the droplet by the high-speed air stream (Theofanous, Li & Dinh 2004). Similar to the breakup observed for high-speed jets (Jarrahbashi *et al.* 2016; Zandian, Sirignano & Hussain 2019), this mechanism has been analysed in terms of the Kelvin–Helmholtz instability (Jalaal & Mehravaran 2014). These mechanisms give reasonable agreement in terms of both the physical process of atomization as well as the mean sizes of the breakup at very high *We*; however, these mechanisms are not relevant to the present work, which focuses on the breakup at low *We*.

One of the main issues in modelling low-*We* droplet breakup is that there are three dominant geometries that contribute to the breakup: the rim, the bag and the undeformed core. The process is further complicated by the formation of large nodes on the rim of the droplet prior to the breakup (Chou, Hsiang & Faeth 1997), as well as the potential breakup of the undeformed core. As a result of these varied geometries, the resulting size distribution for low-*We* droplet breakup is typically multimodal (Chou *et al.* 1997; Guildenbecher, López-Rivera & Sojka 2009; Guildenbecher *et al.* 2017). Although several empirical works have studied all modes simultaneously, most analytical works focus on only one at a time.

The only work to analytically study the formation of node drops is that of Zhao *et al.* (2010), where it was assumed that the mechanism by which the nodes form is due to a Rayleigh–Taylor instability. In the work of Zhao *et al.* (2010), only the number of nodes formed around the rim were predicted by the developed model and no prediction was

made for the sizes, or variation in sizes, of the drops that result from the breakup of the nodes.

The rim of the deformed droplet is the most commonly studied geometry in the breakup as it typically contains a majority of the volume of the droplet, and thus is the most dominant mode of the breakup. Chou *et al.* (1997) were the first to study the rim breakup analytically, and proposed that the mechanism of the rim's breakup was the Rayleigh–Plateau instability, with good agreement with mean measurements of the rim child droplet sizes. Under this view, the rim is assumed to be approximated by a slender liquid column with periodic symmetry; however, the effect of the periodic symmetry is typically neglected in the analyses. The same model was used by Jackiw & Ashgriz (2021) for the breakup of the rim where it was found to slightly over-predict the mean sizes, although the agreement was reasonable. Obenauf & Sojka (2021) also considered the Rayleigh–Plateau instability for the breakup of the rim, but included modifications to account for the possible generation of Hill's vortices in the droplet periphery that result in a vortex within the rim that makes it slightly more stable. Despite reasonable agreement of their model with their results, there is no verification of the existence of Hill's vortices inside droplets at low *We* in the literature. Such vortices have been observed for droplets falling at terminal velocity where the flow time scales are large; however, in the present case of aerodynamic droplet breakup, the breakup time scale is expected to be shorter than the time required for the vortices to develop (Rimbert *et al.* 2020). Numerical simulations such as those of Jain *et al.* (2019) have revealed no significant vortex flow either in the periphery of the deformed drops or in the rim. Furthermore, it is noted in Jackiw & Ashgriz (2021) that the receding bag impacts the rim of the droplet, which may also contribute to the rim's breakup dynamics.

The breakup of the bag in aerodynamic droplet breakup is considerably more difficult to study compared to the breakup of the rim due to the large range of scales at play in its dynamics. The droplets ejected from the breakup of the bag are of the order of micrometres while the size of the bag is of the order of millimetres. Furthermore, the bag moves with the droplet throughout the breakup. Consequently, a very high spatial resolution along with a large field of view are necessary to properly study the dynamics of the bag, which are difficult to attain simultaneously. Due to these challenges, there are no works to date that study the breakup of the bag in aerodynamic droplet breakup. There are many studies that consider the similar geometry of a surface bubble; however, the applicability of these works to the breakup of the bag in aerodynamic droplet breakup has not been examined.

The breakup of the undeformed core has not been studied explicitly; however, it is reasonable to assume that it undergoes a similar phenomenon to the breakup of the parent droplet, albeit at a smaller size and relative speed.

While there have been many works that have studied many of the individual aspects of aerodynamic droplet breakup, there remain several mechanisms that have not been studied, such as the formation and breakup of the rim nodes, the collision of the bag with the rim and the breakup of the bag. Furthermore, the models developed for the breakup of the rim have only provided predictions of the mean droplet size, with no mechanistic origin for the variation in sizes that result in the distribution of the breakup from each mode.

The only analytical work to consider the distribution in sizes is that of Villermaux & Bossa (2009), who provided a single-parameter gamma distribution using an empirical fit to their data. The fit is based on their earlier work (Villermaux, Marmottant & Duplat 2004) where the source of variation is assumed to be random corrugations in the initial ligament. Therefore, their work does not consider the interplay and summation of the
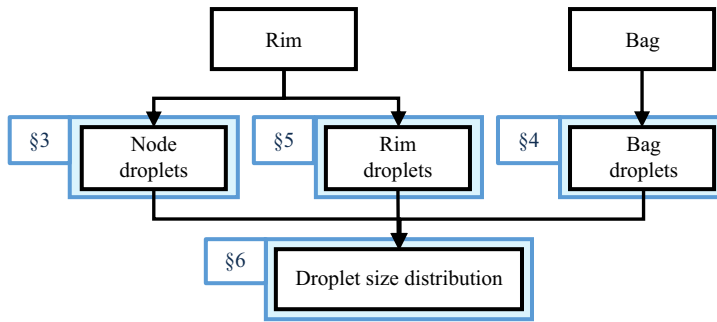
Figure 2. Flowchart of the present paper. Blue boxes denote the relevant sections of the present work.

various geometries and their breakup mechanisms, which contribute to the distribution of sizes.

The distribution in the breakup sizes from aerodynamic droplet breakup is the result of the combination of several modes of breakup, each with a plethora of potential breakup mechanisms that contribute to the variation in the breakup sizes. Several of these modes and mechanisms have not been modelled previously and their sources of variation have not been identified. Furthermore, their combination to give the overall child droplet size distribution has not been considered. The present work seeks to address these issues.

The aims of this work are as follows:

  (i) Identify the dominant mechanisms in the breakup of the rims and bags in aerodynamic droplet breakup.
 (ii) Model the dominant mechanisms to predict the characteristic sizes of each mechanism and how they vary.
(iii) Develop a model for the droplet size distribution resulting from aerodynamic breakup, considering the plurality of breakup mechanisms.

While our earlier work provided a detailed analysis of the initiation phase of the droplet breakup with a simplified analysis of the breakup phase, the present work provides a more detailed analysis of the dynamics that govern the breakup of the rim and bag in aerodynamic droplet breakup after the initiation phase.

In § 3, the dynamics of the node formation in the rim is studied and a model is developed to predict the node droplet sizes as well as their variation. In § 4, the dynamics of the breakup of the bag is studied using existing methodologies developed for the bursting of surface bubbles. While the actual child droplet sizes of the bag are not determined in the present experiments, predictions of the characteristic sizes as well as their variation are given. In § 5, the breakup mechanisms of the rim are studied and modelled, including both the established Rayleigh–Plateau instability mechanism as well as the mechanism of the collision of the bag with the rim, to give predictions of child droplet sizes resulting from the breakup of the rim. Finally, in § 6, the models for the node, bag and rim child drops are combined to develop a method of estimating the droplet size distribution resulting from aerodynamic droplet breakup. The results are compared with the detailed measurements of Guildenbecher *et al.* (2017). Figure 2 gives a flowchart to graphically represent the present work.

940 A17-6

We	Frame rate (kHz)	Shutter speed (ms)
7.6–28	20	1/91
40–167	42	1/89
152	50	1/99
133–200	60	1/150

Table 1. Camera settings.

2. Experiments

Droplets having an initial diameter $d_0 = 1.9 \pm 0.2$ mm were generated and suspended by a 30 gauge needle (outer diameter of 0.305 mm) fed by a syringe pump (SyringePump.com NE-1000). The pendant drops were positioned at the outlet of a 5 gauge needle (inner diameter of 5.7 mm) 60 mm in length to which the building's compressed air supply, at 100 psi, was connected to generate an air jet from the nozzle tip. A gas-flow rotameter (Matheson FM 1050 E700 for flow rates of 13.75–30 LPM, Cole Parmer 03217-34 for flow rates of 30–68 LPM) and a pressure transducer (WIKA A-10) were used to measure and calculate the steady-state average airflow speed, U, which ranged from 16.7 to 78.4 m s^{-1}, to which the pendant droplet was exposed. The needle valve of the gas-flow rotameter was used to set the steady-state flow rate through the system, and a solenoid immediately upstream of the air needle was used to suddenly start air jet. Water was used as the liquid for the pendant drops and the air jet was assumed to issue at atmospheric conditions. The liquid and air properties were thus taken as $\rho_l = 1000$ kg m^{-3}, $\mu_l = 1.0$ mPa s, $\rho_g = 1.2$ kg m^{-3} and $\sigma = 0.0729$ N m^{-1}. The droplet breakup was studied for the conditions $7.3 < We < 200$ and $Oh = 0.0027$ over 96 experimental runs. A high-speed camera (Photron Fastcam SA-5 1000 K-M3) with a spatial resolution of approximately 0.0431 mm pixel^{-1} was used to study the droplet breakup process using a shadowgraphy configuration, backlit by a constant-source floodlight (Dedolight DLHM4-300 U). The settings of the camera were varied based on the requirements for each set of flow conditions and are tabulated in table 1. The child droplet sizes were measured from the images using the ImageJ particle size measurement tool.

The experimental facility and primary data (i.e. the high-speed videos) are identical to those of our previous work. For further details, see Jackiw & Ashgriz (2021).

3. Rim dynamics

After the rim has formed at the end of the initiation deformation, it continues to grow and be stretched by the action of the inflating bag. Throughout this stretching, large 'nodes' form around the rim of the droplet, as shown in figure 3. These nodes start forming due to an instability on the rim shortly after its initiation. Upon breakup, the nodes separate into distinct droplets that are the largest characteristic size in the breakup. The node child droplet sizes are therefore related to the dominant wavelength of the instability mechanism that causes their formation.

Previous investigations of the mechanism of node formation have assumed the node instability to be of a Rayleigh–Taylor type (Zhao *et al.* 2010). The Rayleigh–Taylor instability is used for describing the aerodynamic droplet breakup process due to the acceleration of the droplet in the air stream (Joseph *et al.* 2002; Theofanous *et al.* 2004; Zhao *et al.* 2010), and thus it is natural that this theory should also be expected to dominate
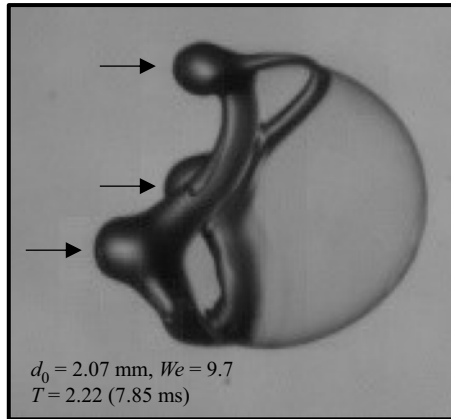
Figure 3. Image showing the nodes on the rim of a deformed water droplet. The arrows denote the nodes formed on the rim, $N = 3$. See supplementary movie 1.

the node formation in the rim. However, it is also possible that a Rayleigh–Plateau type of instability causes the rim's corrugation owing to its cylindrical shape, which is susceptible to capillarity. Furthermore, previous investigations have only considered the number of nodes formed around the rim, N, and not their resulting breakup size, d_N.

In this section, both Rayleigh–Taylor and Rayleigh–Plateau theories are compared in the formation of the rim nodes. The aim of this analysis is to develop a more complete prediction of the rim dynamics to predict both N and d_N, as well as to identify the root cause of the variability in d_N (i.e. the distribution of sizes resulting from the breakup) and the dimensions of the rim that remains between the nodes.

3.1. *Rim node instability*

3.1.1. *The Rayleigh–Taylor instability*

Zhao *et al.* (2010) suggest that the rim nodes are the result of a Rayleigh–Taylor instability on the rim, which has a maximum susceptible wavelength, λ_{RT}, of

$$\lambda_{RT} = 2\pi\sqrt{\frac{3\sigma}{\rho_l a}}, \tag{3.1}$$

where a is the acceleration of the deforming droplet. The acceleration a can be estimated by considering the drag force on the flattened droplet as

$$a = \frac{3}{4}C_D\frac{U^2}{d_0}\frac{\rho_g}{\rho_l}\left(\frac{2R}{d_0}\right)^2, \tag{3.2}$$

where C_D is the drag coefficient of the flattened droplet and $2R/d_0$ is the extent of the droplet deformation at the instant the instability takes hold. Upon substitution, the wavelength of the Rayleigh–Taylor instability on the liquid rim is

$$\frac{\lambda_{RT}}{d_0} = \frac{4\pi}{\sqrt{C_D We}}\left(\frac{d_0}{2R}\right). \tag{3.3}$$

Although this expression was derived to predict the instability wavelength over the whole droplet with the aim of modelling the Rayleigh–Taylor piercing breakup mechanism

at very high *We* (Theofanous *et al.* 2004), Zhao *et al.* (2010) argued that the same analysis can also be used to predict the instability wavelength of the rim.

From (3.3), the two undetermined variables are C_D and $2R$. Physically, the drag coefficient can vary between that of a sphere ($C_D = 0.4$) and that of a disk ($C_D = 1.2$). Since the highest acceleration will occur when the droplet takes the approximate shape of a disk, the value $C_D = 1.2$ is practical for the case of the Rayleigh–Taylor instability.

Zhao *et al.* (2010) assume that the instability takes hold when the droplet reaches its maximum cross-sectional deformation, R_{max}, prior to bag blow-out, which is slightly after the rim is initiated. Zhao *et al.* (2010) provided the following correlation for R_{max}:

$$\frac{2R_{max}}{d_0} = \frac{2}{1 + \exp(-0.0019We^{2.7})}. \tag{3.4}$$

In the analysis of Zhao *et al.* (2010), the correlation used for the prediction of N is that of Hsiang & Faeth (1992) ($2R_{max}/d_0 = 1 + 0.19\sqrt{We}$); however, the correlation given by (3.4) provides a more consistent prediction of N, as is shown later in this section.

3.1.2. *The Rayleigh–Plateau instability*

The Rayleigh–Plateau instability wavelength, λ_{RP}, depends only on the thickness of the rim at its initiation, h_i (i.e. the minor diameter of the toroidal rim), as (Rayleigh 1878)

$$\frac{\lambda_{RP}}{d_0} = 4.5\frac{h_i}{d_0}, \tag{3.5}$$

where it is assumed that the rim is approximately a cylinder with periodic symmetry. The thickness h_i is given by our previous model (Jackiw & Ashgriz 2021); however, in the present work, we consider a minor modification to the model, which is discussed in detail in Appendix A. The model for h_i is given by

$$\frac{h_i}{d_0} = \frac{4}{We_{rim} + 5\left(\frac{2R_i}{d_0}\right) - 4\left(\frac{d_0}{2R_i}\right)} - 0.05, \tag{3.6}$$

where $We_{rim} = \rho_l \dot{R}^2 d_0/\sigma$ is the rim *We*, for which $\dot{R}$ is given by

$$\frac{2\dot{R}}{d_0} = \frac{1.125}{\tau}\left(1 - \frac{32}{9We}\right). \tag{3.7}$$

The modification to the model is in the definition of the cross-sectional deformation at initiation, $2R_i$, which is now given by the following empirical relation (see (A1)):

$$\frac{2R_i}{d_0} = 1.63 - 2.88\exp(-0.312We). \tag{3.8}$$

Other combinations of the instability theories and extents of deformation are compared in Appendix B. The two presented here are the most reasonable and accurate of the possible combinations for both the Rayleigh–Taylor and Rayleigh–Plateau instabilities.

3.1.3. *Instability breakup time*

The first comparison of the plausibility of the Rayleigh–Taylor and Rayleigh–Plateau instabilities in the formation of the rim nodes is in the comparison of their characteristic

breakup times, t_b. The breakup time of a liquid column is found by the time required for an initial perturbation to grow to the radius of the column, given by Grant & Middleman (1966) and Ashgriz (2011)

$$t_b = \frac{C_t}{\omega_{max}}, \tag{3.9}$$

where $C_t = \ln((h_i/2)/\zeta_0)$ is a constant related to the initial perturbation, ζ_0, and the radius of the column, $(h_i/2)$, and ω_{max} is the growth rate of the most unstable wave. Since ζ_0 is very small ($O(nm)$), C_t must be determined experimentally. As a point of reference, Grant & Middleman (1966) give $C_t = 13$ for the breakup of a laminar jet by the Rayleigh–Plateau instability.

The maximum susceptible growth rates for the Rayleigh–Taylor, $\omega_{max,RT}$, and Rayleigh–Plateau, $\omega_{max,RP}$, instabilities are given by

$$\omega_{max,RT} = \left(\frac{a^3 \rho_l}{2\sigma}\right)^{1/4} \tag{3.10}$$

and

$$\omega_{max,RP} = 0.97\sqrt{\frac{\sigma}{\rho_l h_i^2}}, \tag{3.11}$$

respectively (Chandrasekhar 1961). The acceleration, a, is estimated using (3.2). Additionally, the value of $2R_{max}$ used in the Rayleigh–Taylor theory is calculated using (3.4). The definition of the maximum deformation, $2R_{max}$, is somewhat subjective as it depends on identifying the first instance that the bag blows out behind the deformed droplet; therefore the empirical correlation of Zhao *et al.* (2010) (equation (3.4)) is used to be consistent with their work. All other inputs to (3.10) and (3.11) can be pragmatically identified and measured directly from experiments.

The characteristic breakup times for both the Rayleigh–Taylor and Rayleigh–Plateau instabilities are compared with the experiments in figures 4(*a*) and 4(*b*), respectively, where the experimental t_b is measured as the time between the initiation of the rim (T_i, i.e. when the rim first forms and becomes susceptible to the instability) and the end of the breakup of the rim (i.e. when the instability fully penetrates and fragments the rim). Note that this definition is slightly complicated by the fact that it considers the breakup of the remaining rim between the nodes rather than of just the nodes themselves. This is necessary in the present analysis since the nodes do not typically fragment before the remaining rim. For this reason, the comparison of the instability breakup times is only approximate to test if the theoretical breakup times are within a reasonable range.

The values of C_t for both the Rayleigh–Taylor and Rayleigh–Plateau instabilities are obtained by fitting (3.9) (using (3.10) and (3.11) for the Rayleigh–Taylor and Rayleigh–Plateau cases, respectively) to the data, giving $C_t = 7.1$ ($r^2 = -0.04$) and $C_t = 4.1$ ($r^2 = 0.55$) for the Rayleigh–Taylor and Rayleigh–Plateau instabilities, respectively. Both fitted values of C_t are of the same order of magnitude as that given by Grant & Middleman (1966), and also give $\zeta_0 = O(nm)$, suggesting that both theories are reasonably plausible given the potential experimental error in t_b and the increased perturbation due to the aerodynamic forces on the droplet and the rim. Although the Rayleigh–Taylor theory follows the data well for the BS morphology, the theory sharply over-predicts the breakup time through the bag morphology, resulting in $r^2 < 0$ for the whole fit. This likely arises due to the much smaller cross-sectional deformation that occurs in this regime
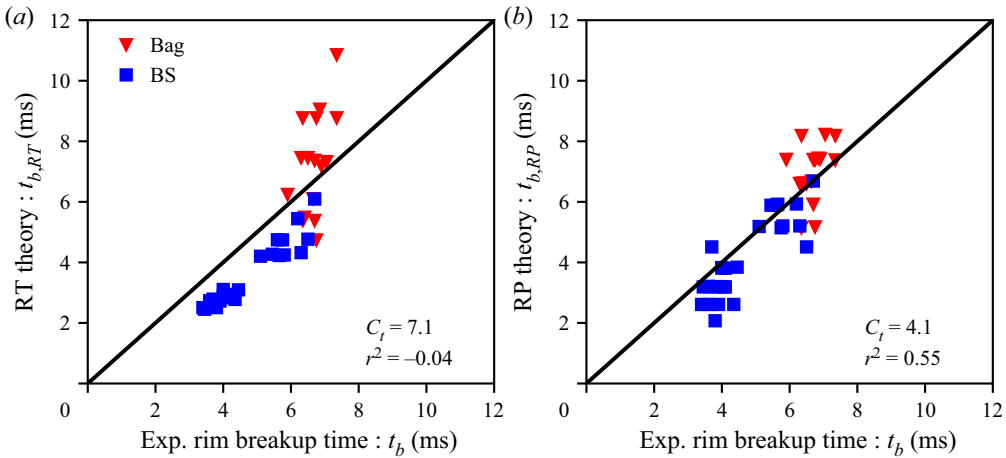
Figure 4. Comparison of the theoretical breakup time with the experimental breakup time for the (*a*) Rayleigh–Taylor ((3.9) given (3.10)) and (*b*) Rayleigh–Plateau ((3.9) given (3.11)) instability theories. The constant C_t is fitted to the experiments for both cases.

(see (3.4)), which has a strong effect on the prediction of the acceleration, $a \propto (2R/d_0)^2$. However, we again stress that due to the challenges in estimating the experimental breakup time of the nodes compared with the rest of the rim, the comparison of the instability breakup times is only approximate and is meant to test if the theoretical breakup times are within a reasonable range.

3.2. *Comparison of instability theories for rim node dynamics*

Having shown that the Rayleigh–Plateau theory is equally as plausible as the well-used Rayleigh–Taylor theory for the instability of the rim that forms the nodes, we now turn to the prediction of the number of nodes formed (§ 3.2.1) and their size upon breakup (§ 3.2.2).

3.2.1. *Node formation: number of nodes*

Assuming that the toroidal rim is unstable to a wavelength λ, then the number of nodes, N, formed around the rim will be equal to the whole number of wavelengths that can fit around the circumference of the deformed droplet (Zhao *et al.* 2010):

$$N = \pi \frac{2R}{\lambda}. \tag{3.12}$$

For the case of the Rayleigh–Taylor instability, the substitution of (3.3) into (3.12) yields

$$N_{RT} = \pi \frac{2R_{max}}{\lambda_{RT}} = \frac{\sqrt{C_D We}}{4} \left(\frac{2R_{max}}{d_0} \right)^2. \tag{3.13}$$

For the case of the Rayleigh–Plateau instability, the substitution of (3.5) into (3.12) yields

$$N_{RP} = \pi \frac{2R_{max}}{\lambda_{RP}} = \frac{\pi}{4.5} \frac{2R_{max}}{d_0} \frac{d_0}{h} \approx 0.69 AR, \tag{3.14}$$

where $AR = 2R_{max}/h$ is the aspect ratio of the toroidal rim. Note that in this case, the maximum deformation, $2R_{max}$, has been used instead of the initiation deformation, $2R_i$.
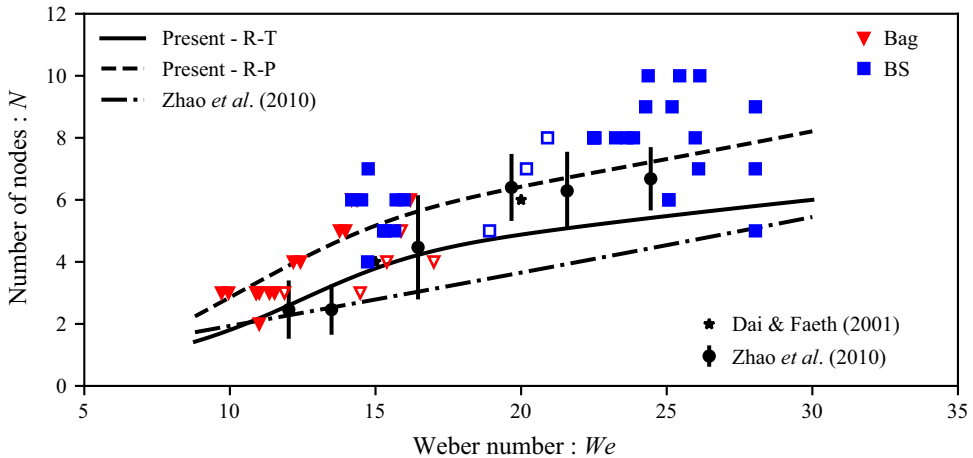
940 A17-11

Figure 5. Comparison of the present Rayleigh–Taylor (equation (3.13)) and Rayleigh–Plateau (equation (3.14)) models for number of nodes, N, versus We compared with the present experiments for water droplets as well as the measurements of Dai & Faeth (2001) and Zhao *et al.* (2010) for water and ethanol droplets and the semi-empirical model of Zhao *et al.* (2010). Filled and open markers indicate results from side- and end-on-view experiments, respectively.

This is because while the instability is set up by the thickness of the rim at initiation, by the time the instability has grown enough to bifurcate the nodes of the rim, the rim has expanded closer to its maximum deformation. The rim thickness does not change significantly in the early stages of its expansion, and therefore the initiation thickness still governs the Rayleigh–Plateau instability (equation (3.5)) at the maximum deformation. Further detail is given in Appendix B.1.

Equations (3.13) and (3.14) are compared with the experimental measurements of the present analysis as well as the measurements of Dai & Faeth (2001) and Zhao *et al.* (2010), which consist of water and ethanol droplet experiments, and the semi-empirical model of Zhao *et al.* (2010) in figure 5. Note that while the models are shown as continuous in N, they represent discrete steps in N, as N must be a whole number due to the azimuthal symmetry condition of the toroidal rim.

Both models are found to follow the trend of the data and lie within its variability, with the Rayleigh–Taylor model (equation (3.13)) generally predicting the lower extent and the Rayleigh–Plateau model (equation (3.14)) generally predicting the mean. This suggests that the Rayleigh–Plateau instability may be more appropriate for modelling the instability of the rim than the Rayleigh–Taylor instability; however, considering the variation in N for both the present data and that of Zhao *et al.* (2010) as well as the variation about the correlations for the extent of deformation ((3.4) and (3.8)), the results of figure 5 do not conclusively distinguish which mechanism is truly dominant. One of the possible causes for the experimental variation in N is the coupling effect of the bag structures that form behind the droplet. For instance, in the BS morphology, the stamen can cause the bag to lose symmetry by inducing a fold in the bag (i.e. the beginnings of 'twin-bag' breakup; Jackiw & Ashgriz 2021), which may affect the symmetry of the rim, and thus its instability. Furthermore, the present Rayleigh–Taylor prediction, which uses the empirical correlation of Zhao *et al.* (2010) for $2R_{max}$, provides a better prediction of the trend than the Rayleigh–Taylor prediction of the same work, which instead uses the empirical correlation
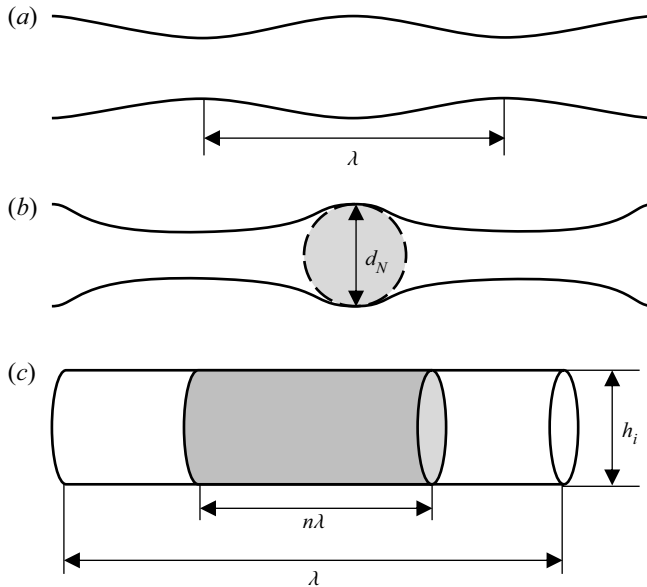
Figure 6. Illustration of node formation due to rim instability of wavelength λ showing (*a*) the initial corrugation of the rim, (*b*) the formation of a node and (*c*) the assumed geometry of a cylindrical wavelength segment. The shaded areas denote the node volume.

of Hsiang & Faeth (1992). This highlights the importance of accurately modelling the extent of deformation on the downstream predictions such as *N*.

Note that the models presented here are simplified and neglect several potentially stabilizing effects. These effects are discussed further in Appendix B.1 and it is noted that these effects can only be compared with the present cases qualitatively.

3.2.2. *Node breakup: node child droplet size*

Once the nodes have formed on the rim of the droplet, they persist until the rim breaks, at which time they will break from the rim as child droplets having a size significantly larger than those formed by the rest of the rim. If all of the liquid contained within each wavelength on the liquid rim goes into the resulting droplets, then there would be no rim remaining after the node breakup. However, this is not what is observed, as a thinned region that undergoes its own breakup does remain between the nodes, likely due to nonlinear flow dynamics within the thin ligaments during the expansion of the rim. This is illustrated in figures 6(*a*) and 6(*b*). Therefore, it is only some fraction of the volume contained in each wavelength that contributes to the node child drops.

By conservation of mass between a node droplet and the fraction *n* of the cylindrical wavelength segment of the rim having diameter h_i and length λ, as illustrated in figure 6(*c*), the rim child droplet size is found as

$$\frac{d_N}{d_0} = \left[\frac{3}{2} \left(\frac{h_i}{d_0} \right)^2 \frac{\lambda}{d_0} n \right]^{1/3}, \tag{3.15}$$

where h_i is given by (3.6) and λ is given by (3.3) and (3.5) for the Rayleigh–Taylor and Rayleigh–Plateau instabilities, respectively. For $n = 1$, the entire wavelength segment will convert into the node child droplet. The problem, then, turns to determining how much of

a given wavelength segment becomes part of the node (i.e. determining the appropriate value for n), and thus the node child droplet.

Since n is the volume fraction of a wavelength segment of the rim that results in a node, n must also be the fraction of the total volume of the rim that results in all of the nodes. Therefore, $V_N = nV_r$, where V_N is the total volume of the node droplets and V_r is the total rim volume. Assuming that the total volume of the rim does not change after its initiation, then one can use the expression provided by Jackiw & Ashgriz (2021) for the volume contained in the rim at the initiation geometry as

$$\frac{V_r}{V_0} = \frac{3\pi}{2}\left[\left(\frac{d_i}{d_0}\right)\left(\frac{h_i}{d_0}\right)^2 - \left(\frac{h_i}{d_0}\right)^3\right]. \tag{3.16}$$

Figure 7(a) plots the fraction of the total measured node volume (i.e. the sum of the node child droplet volumes) against the rim volume estimated by (3.16), where the dimensions of the rim are measured from experiments. The results show that under the assumption that the rim volume is constant after its initiation the node drops should account for roughly 90 % of the rim volume ($n = 0.9$). However, this result is not physically accurate, as the remainder of the rim does not thin sufficiently to only account for 10 % of the total rim volume. Furthermore, the result $V_N/V_r > 1$ is not physical if it is assumed that there is no flow between the inner portion of the disk and the rim. This suggests that liquid continues to feed the rim from the windward disk after the rim's initiation. Essentially, it is suggested that as the nodes draw liquid from the remaining rim, the remaining rim in turn draws liquid from the inner portion of the windward disk in order to maintain its equilibrium shape for as long as possible. As such, the rim scavenges liquid from the windward disk, and thus the total rim volume is better represented by the total volume of the windward disk, V_d. These flows are illustrated in figure 8. Jackiw & Ashgriz (2021) give an expression for the volume of the windward disk as

$$\frac{V_d}{V_0} = \frac{3}{2}\left[\left(\frac{d_i}{d_0}\right)^2\left(\frac{h_i}{d_0}\right) - 2\left(1 - \frac{\pi}{4}\right)\left(\frac{d_i}{d_0}\right)\left(\frac{h_i}{d_0}\right)^2\right]. \tag{3.17}$$

Figure 7(b) shows that the mean volume of the nodes relative to the windward disk is $V_N/V_d \approx 0.4$, while the minimum volume is $V_N/V_d \approx 0.2$. As given earlier, the maximum physical value is $V_N/V_d \approx 1$. Assuming that a majority of the liquid in the windward disk will eventually contribute to the rim, then the volume fraction of the nodes relative to the windward disk will be representative of the volume fraction of the wavelength segment that becomes the node, $V_N/V_d \approx n$. Therefore, the minimum, mean and maximum values of n are $n \approx 0.2$, $n \approx 0.4$ and $n = 1$, respectively.

Using these values of n and assuming the Rayleigh–Taylor (equation (3.3)) and Rayleigh–Plateau (equation (3.5)) wavelengths, (3.15) is compared with the experimental data in figures 9(a) and 9(b), respectively.

Figure 9 shows that both the Rayleigh–Taylor and Rayleigh–Plateau instability theories with (3.15) give reasonable prediction of the range of node droplet sizes in the present experiments, where the mean node volume fraction, $n = 0.4$, predicts the mean trend of the node breakup sizes, d_N, and the maximum and minimum values of $n = 1$ and $n = 0.2$, respectively, capture the upper and lower limits of the spread of d_N. Firstly, this indicates that the present analyses well represent the node formation and breakup process. Secondly, the variation in the node volume fraction, n, is a good indicator of the variation in sizes produced.
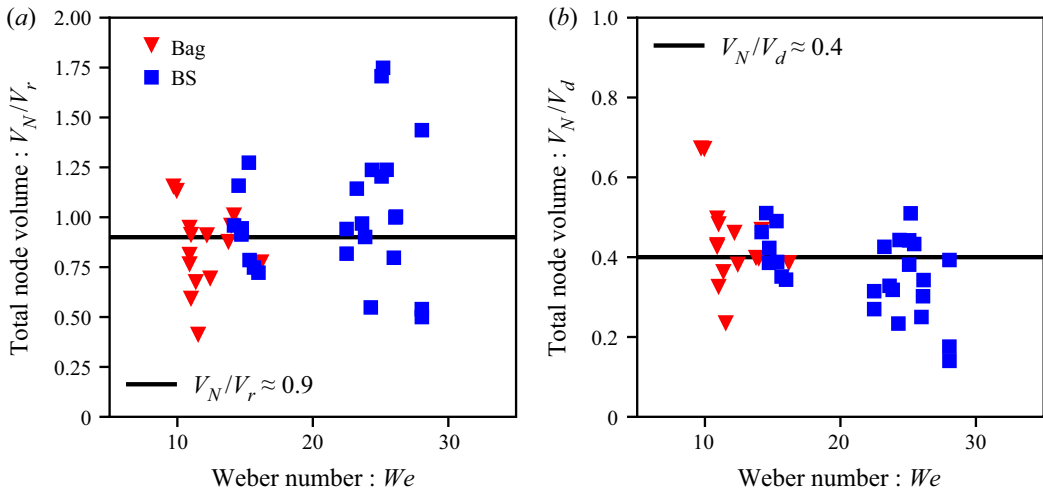
Figure 7. Node volume versus *We* relative to (*a*) the predicted volume of the rim (equation (3.16)) and (*b*) the predicted volume of windward disk (equation (3.17)).
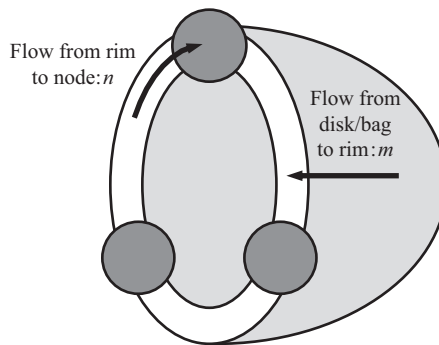

Figure 8. Illustration of the flows in the rim formation process, where liquid flows from the centre of the windward disk into the rim and from the rim into the disk.
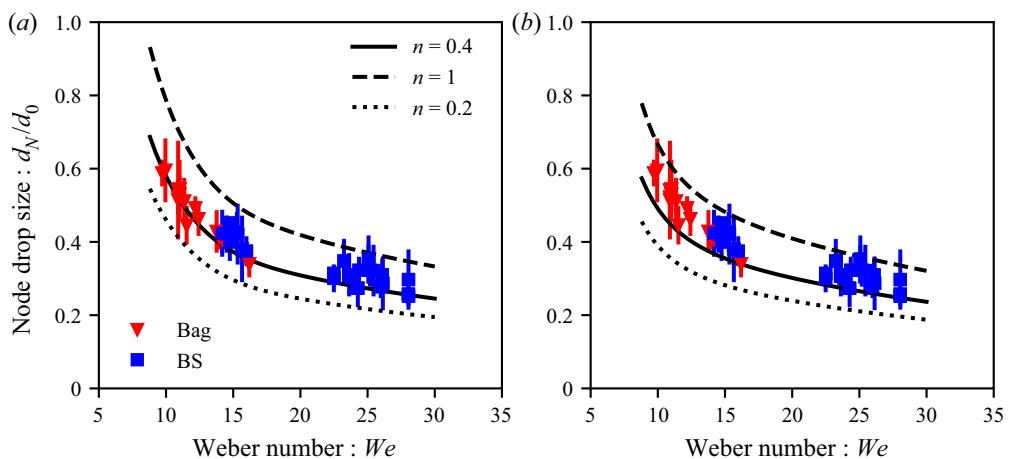

Figure 9. Node child droplet size versus *We* compared to predictions of the (*a*) Rayleigh–Taylor (equation (3.3)) and (*b*) Rayleigh–Plateau (equation (3.5)) mechanisms.

940 A17-15

The predictions of the Rayleigh–Taylor and Rayleigh–Plateau instability theories are very similar. The Rayleigh–Taylor theory predicts d_N somewhat better than the Rayleigh–Plateau theory, which slightly under-predicts the mean trend; however, the difference may be explained by the instability taking hold slightly after the rim is initiated, which would slightly reduce h_i (3.6) owing to the thinning of the rim, and thus reduce the prediction of d_N. Identifying the instant that the instability takes hold, in particular in the time between the initiation (*i*) and the maximum (*max*) extents of deformation, is not possible from the present experiments as the rim is not resolved with enough detail and dimension to quantify the development of its corrugation in the early stages of the instability. The results of figure 9 are therefore not sufficient to conclude which instability is truly dominant; however, at this time, the Rayleigh–Taylor instability theory appears to give the most accurate results for d_N in the present experiments.

It is of note that the difference in the prediction of the Rayleigh–Taylor and Rayleigh–Plateau theories for N is greater than for d_N (compare figures 5 and 9). Although these two quantities could be well correlated if d_N were derived from volume conservation for the whole rim, the derivation used here only considers volume conservation in one wavelength segment of the rim. As a result, N and d_N are not directly related to each other; however, they are related indirectly through the rim geometry parameters, $2R$ and h (note that λ is itself dependent on $2R$ and h). Comparing the predictions of N ((3.13) and (3.14) for the Rayleigh–Taylor and Rayleigh–Plateau theories, respectively) with the predictions of d_N (equation (3.15)), it can be seen that d_N is less sensitive than N to $2R$. Since the Rayleigh–Taylor and Rayleigh–Plateau theories are each better suited to a different definition of $2R$, the difference between the models for N is greater than for d_N.

3.3. *Remarks on the rim node instability*

In the literature, the only instability that is considered in the growth of the rim nodes is the Rayleigh–Taylor instability (Zhao *et al.* 2010; Xu, Wang & Che 2020; Qian *et al.* 2021); however, in the present work, it was found that the Rayleigh–Plateau instability theory gives comparable results with those of the Rayleigh–Taylor instability in terms of breakup time, number of nodes formed and the resulting breakup sizes of the node drops. In terms of the breakup time and the number of nodes formed, the Rayleigh–Plateau theory was found to provide a slightly better prediction than the Rayleigh–Taylor theory, while for the final breakup size of the nodes, the Rayleigh–Taylor theory provided the better agreement with the experiments. In all cases, however, the variations were small enough that they were easily attributed to experimental errors or to slight variations in the definition of the extent of deformation at which the instability takes hold. As a result, we cannot conclude quantitatively which mechanism is truly occurring in the case of the node formation in the rim. Furthermore, other analyses of the instabilities of rims, such as the rim on the edge of a receding sheet, have also found that the two mechanisms provide similar results in predicting the instability of the rim (Lhuissier & Villermaux 2011; Wang *et al.* 2018). In fact, Lhuissier & Villermaux (2011) concluded that the predictions from these two idealized mechanisms are 'intrinsically undistinguishable'.

Although the results of these two theories may be functionally interchangeable for the present case in terms of a quantitative analysis, it may be instructive for future study to consider the qualitative differences between the two theories. In particular, a potentially severe flaw with the Rayleigh–Taylor instability approach is that it considers no changes to the original derivation for the case of the instability of an infinite planar interface when applied to the finite cylindrical interface of a rim. For the cylindrical rim, the additional

curvature of the surface in the case of a cylindrical (or at least approximately cylindrical) body, in particular the axial curvature, would be expected to have a significant effect on the planar assumption of the applied Rayleigh–Taylor theory. Krechetnikov (2010) showed that the interplay of both the Rayleigh–Taylor and Rayleigh–Plateau mechanisms must be considered in the problem of the instability of a liquid sheet edge. Since the surface tension component stabilizes the Rayleigh–Taylor mechanism while destabilizing the Rayleigh–Plateau mechanism, as the scale of the problem decreases, the Rayleigh–Plateau mechanism becomes dominant. For the case of the rim at the edge of an expanding liquid sheet (i.e. in droplet impact), Wang *et al.* (2018) found that, in most cases, the combined dynamics collapse to those of the Rayleigh–Plateau instability. Although the case of Wang *et al.* (2018) is not directly transferable to the present one, it is illustrative of the effect of the curvature of the rim on the planar assumption of the Rayleigh–Taylor analysis.

In spite of the potential phenomenological downfall of the Rayleigh–Taylor theory described above, it is nonetheless unavoidable that, in the present work, the Rayleigh–Taylor theory gives a somewhat better prediction of d_N. Since the present work aims to develop a relationship for the distribution of droplet sizes originating from the variety of mechanisms of child droplet formation in aerodynamic droplet breakup, we will carry forward the Rayleigh–Taylor model; however, we stress that future works should not overlook the viability of the Rayleigh–Plateau theory for this case, as this mechanism may be more generalizable than the Rayleigh–Taylor theory if sufficient improvement in the modelling of the dynamics can be made.

3.4. *Remaining rim dimensions*

Since the breakup of the remaining rim will depend on its dimensions, it is necessary to determine these dimensions, in particular the thickness. Two factors contribute to the thinning of the rim. Firstly, since the rim major diameter expands in time, it must thin in order to conserve its volume. This is described in Jackiw & Ashgriz (2021), where the rim is found to thin as $h_f/h_i = \sqrt{R_i/R_f}$, where R_f/R_i is the rim expansion ratio through the breakup phase. The second factor is the scavenging of the rim's volume by the formation of the nodes. Since the nodes form from the volume contained in the rim, the remaining rim segments would be expected to have a smaller volume, and thus a smaller thickness, than if the nodes had not formed. The initial and final volumes of the rim are related by the mass fraction remaining in the rim after the nodes have formed, $(1 - n)$, as $V_{r,i}(1 - n) \approx V_{r,f}$, where the rim volume, for either initial or final geometries, is $V_r = \pi^2(2R)h^2/4$.

However, this assumes that the volume of the rim, including the nodes, is constant after its initiation. In the previous section, it was shown that there is some evidence to suggest that liquid continues to flow into the rim after its initiation. We then define an additional parameter, m, that describes the volume fraction of the rim scavenged from the interior portion of the windward disk after the rim's initiation. The mass fraction remaining in the rim accounting for the flow from the interior portion of the windward disk after the nodes have formed is thus $(1 - n + m)$, and $V_{r,i}(1 - n + m) \approx V_{r,f}$. Rearranging and normalizing by the initial droplet volume gives

$$\frac{h_f}{d_0} = \frac{h_i}{d_0}\sqrt{(1 - n + m)\frac{2R_i}{d_0}\frac{d_0}{2R_f}}. \tag{3.18}$$

For $n > m$, more liquid is flowing from the rim to the nodes than is flowing from the windward disk to the rim, while for $n < m$, more liquid is flowing from the windward
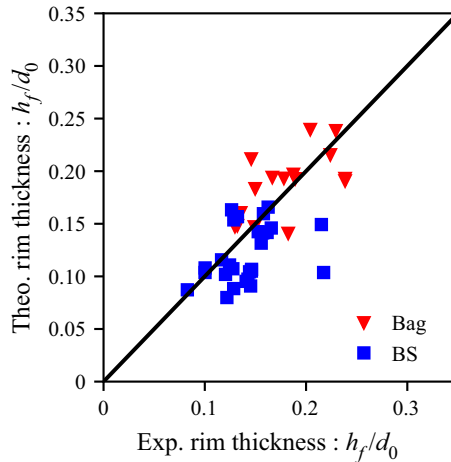
Figure 10. Measured final rim thickness, h_f, compared to the prediction of (3.18) from measurements of h_i and $2R_i$ assuming $n = m = 0.4$.

disk to the rim than from the rim to the nodes. The case of $n = m$ is compared with the measurements in figure 10.

Figure 10 shows that the results of (3.18) for $n = m$ agree well with the present experimental measurements with no obvious dependency on *We* for the studied range of $9 < We < 30$. An increase in n relative to m would result in a lower theoretical prediction, and thus worse agreement with the measurements. Therefore, the earlier suggestion that the rim draws additional liquid from the core of the windward disk after its initiation is supported. Conversely, a small increase in m relative to n may improve the present prediction, suggesting that there is a greater flow from the windward disk into the rim than from the rim into the nodes. Although this suggests an interesting finding in the flow dynamics of droplet breakup, the sensitivity of (3.18) to n and m is relatively small $(O(\sqrt{1 - n + m}))$, and thus, for simplicity in the remainder of the present analysis, the value of $n = m$ is used, recovering the result of Jackiw & Ashgriz (2021) despite the formation of the nodes, which were shown in § 3.2.2 to scavenge $n \approx 0.4$ of the rim's mass.

4. Bag dynamics

The fragmentation of the droplet begins when the bag ruptures. Following its rupture, the bag undergoes phenomenology identical to the bursting of surface bubbles. First, the edge of the bag begins to 'roll up', forming a rim that recedes along the bag. This rim is referred to as the receding rim, denoted by the subscript *rr*. As it recedes, the receding rim becomes susceptible to instability resulting in the formation of nodes along the rim that may digitate and break into a plurality of very small droplets, as shown in figure 11(*b*). The receding rim will continue along the bag until it collides with the main rim or the ligaments formed at the intersection of bags in multibag-type breakups or another receding rim. Although the bursting of static surface bubbles has been studied widely, the knowledge gained from their study has not been compared with the aerodynamic breakup of drops.

In this section, the dynamics of the bag is studied. First, the recession of the bag is used to estimate the the bag thickness throughout the breakup. Then, the instability of the receding rim is compared with a prominent theory for the breakup of films and surface
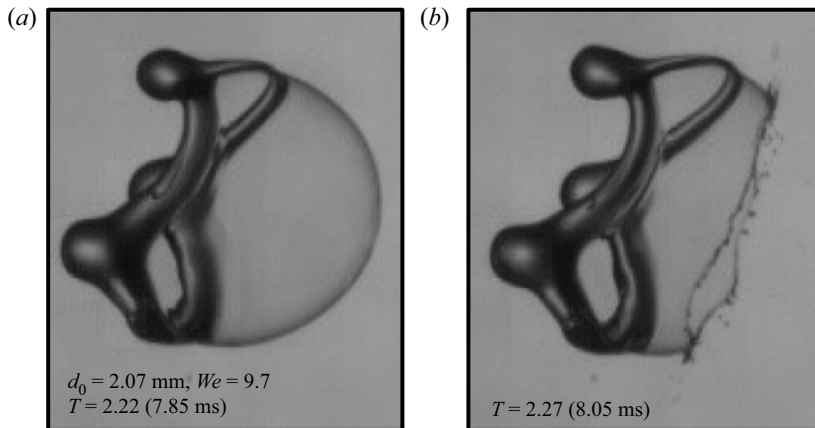
Figure 11. Images of (*a*) the initial bag and (*b*) the rupture and recession of the bag in the breakup of a water droplet, showing the receding rim and the formation of nodes at receding bag edge. See supplementary movie 1.

bubbles to predict the instability wavelength of the receding rim. Finally, using the gained knowledge of the bag dynamics, approximate scaling of the droplet sizes that result from the breakup of the bag is presented.

4.1. *Liquid sheet recession and thickness*

When a liquid sheet ruptures, the curvature of the sheet at the edge of the rupture results in a high surface tension force away from the rupture site, causing the edge of the sheet to recede away from the rupture site. As it does so, the edge of the sheet picks up more liquid from the sheet, forming a rim thicker than the sheet. Culick (1960) showed that these dynamics result in a constant retraction speed, u_{rr}, that depends on the sheet thickness, h, as

$$h = \frac{2\sigma}{\rho_l u_{rr}^2}, \tag{4.1}$$

which is referred to as the Taylor–Culick law. Since the liquid sheet thickness is exceptionally difficult to measure, the Taylor–Culick law is often used to infer the sheet thickness based on the more easily measured retraction speed (Opfer *et al.* 2014; Poulain, Villermaux & Bourouiba 2018; Villermaux 2020).

In the present experiments, u_{rr} is found by measuring the displacement of the edge of the receding rim relative to a relatively stationary point on the deformed droplet, such as the main rim, and taking its derivative. The parallax effect of the curvature of the bag tip is ignored for simplicity. To eliminate the effect of noise on the derivative, the displacement measurement is smoothed using a Savitzky–Golay filter of order 2 for a window length equal to the nearest odd number of measurement points, rounded down. By using this filter, it is assumed that the receding rim experiences a constant acceleration as it recedes, which matches the experiments well as shown in figure 12(*a*). An estimate of the error in the measurement is given by the error bars in figure 12(*a*), assuming that there is an error of ± 2 pixels in identifying both the location of the sheet edge and the reference point (which itself is moving with the droplet), leading to a total error of ± 4 pixels (about 0.17 mm). The bag recession speed is found to decrease linearly with time, indicating based on the
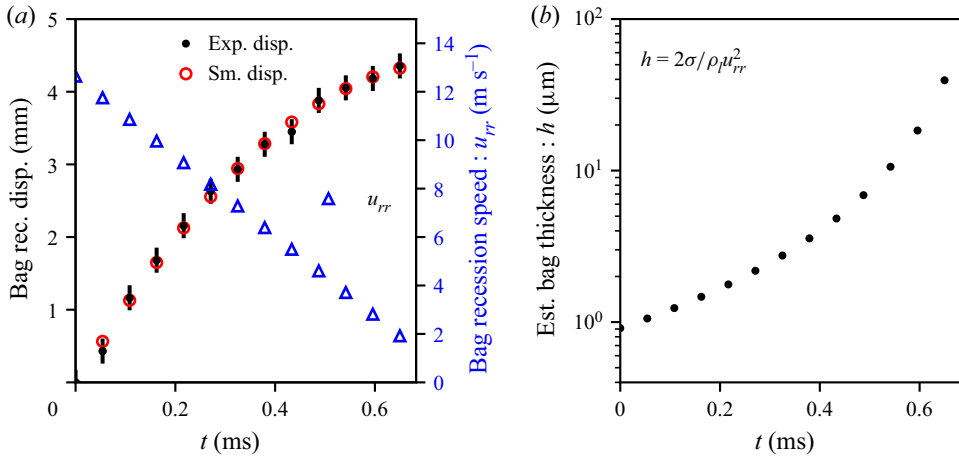
Figure 12. (*a*) Plot of the bag recession displacement in time, comparing experimental measurement with smoothed result using the Savitsky–Golay filter, and the recession speed calculated based on the derivative of the smoothed displacement. (*b*) Estimation of bag thickness based on calculated bag recession speed and Taylor–Culick law (equation (4.1)). Example case for a droplet having $d_0 = 2.07$ mm and $We = 10.1$. Rupture ($t = 0$ ms reference) at $T = 2.08$ (6.95 ms).
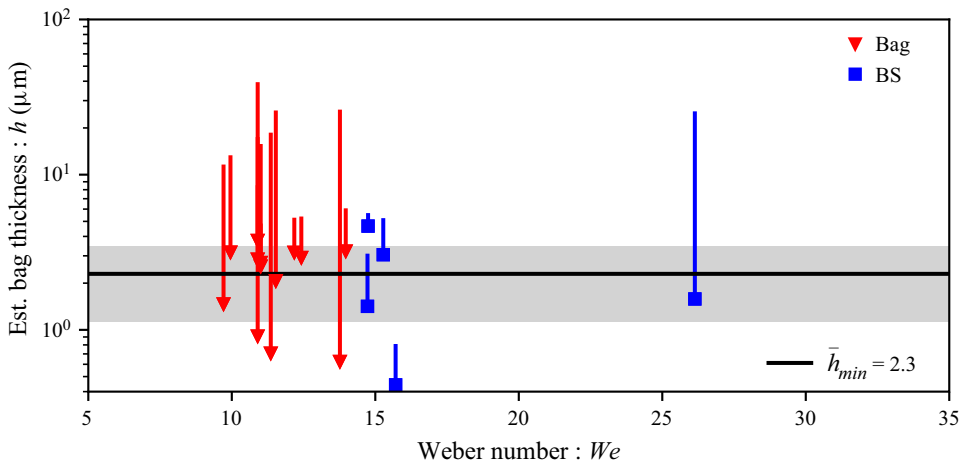

Figure 13. Estimated sheet thickness versus We. Vertical bars show the time variation in h, where h_{min} is indicated by the markers. The shaded region gives the standard deviation of h_{min} across all experiments.

Taylor–Culick law (equation (4.1)) that the bag is thinnest at its rupture site and thickest near the main rim of the deformed droplet, as shown in figure 12(*b*).

The estimated bag thickness results are presented for the present experiments in figure 13, where the markers indicate the minimum thickness and the bars indicate the range of the thickness to its maximum.

The present results indicate that there is no obvious relationship between We and h_{min}, indicating that, at least for the present range of $We < 30$ for water, there is no dependency of h_{min} on We. Opfer *et al.* (2014) found h_{min} to be of a similar order of magnitude ($h_{min} = 1$–0.1 µm over the range $We = 10$–15) despite the initial droplet sizes being approximately $> 50\%$ larger ($d_0 = 3.2$ mm) than in the present study. It is therefore

940 A17-20

reasonable to conclude, given the present results, that there is a universal critical bag thickness at which the bag ruptures for water. Based on figure 13, the average of the minimum bag thickness is $\bar{h}_{min} = 2.3 \pm 1.2$ µm.

Opfer *et al.* (2014) suggested an alternative approach to inferring the evolution of the bag thickness using a conservation of volume argument on the deforming bag where the bag size in the downstream direction at the time of burst is determined empirically. Their results indicated that the bag thickness decreases with increasing *We* from $h_{min} = 1$ to 0.1 µm over the range $We = 10$ to 15 and was found to be independent of the liquid properties over their tested range ($\mu_l = 1$–16.1 mPa s, $\sigma = 21.2$–72 mN m^{-1}). The *We* dependency of the bag thickness is inherited from the *We* dependency of the bag size at burst, which increases with *We* over their tested range. While their prediction of the evolution of the bag thickness coincides with corresponding measurements using the Taylor–Culick sheet recession method, it assumes that mass is conserved in the bag throughout its deformation, to which evidence to the contrary was presented in section § 3.4. While the trend in the bag thickness results of Opfer *et al.* (2014) is contrary to the constant value found in the present work, the order of magnitude and spread of their data is consistent with the present results. Since the actual mechanisms leading to the bag's rupture, and thus its terminal thickness, are still unknown, the present analysis will continue with the constant minimum bag thickness found earlier; however, the work of Opfer *et al.* (2014) highlights the need for further study of the mechanisms of the bag's rupture.

The dynamics governing the rupture of surface bubbles considers, mainly, the competing effects of evaporation (which occurs at times scales > 10 s) and film drainage at the meniscus of the bubble–surface interface (Bourouiba 2021). In some cases, Marangoni flows induced near the meniscus by variations in surfactant concentration or temperature can also affect the lifetime of the bubble (Poulain *et al.* 2018). However, all of these effects have been studied at the relatively long time scales of surface bubble lifetimes ($O(1\text{s})$) as compared with the lifetime of the bag in aerodynamic droplet breakup ($O(\text{ms})$) and do not account for the rapid stretching of the bag. Previous analyses of aerodynamic bag breakup have assumed that the bag ruptures when it develops a Rayleigh–Taylor instability at its tip that results in the piercing of the bag (Vledouts *et al.* 2016; Jackiw & Ashgriz 2021); however, this theory depends on *We* and over-predicts the present results by an order of magnitude.

4.2. *Instability of the receding rim*

Having a view of the bag thickness and recession characteristics, the instability of the receding rim can now be studied. Here, we compare the universal rim thickness criterion of Wang *et al.* (2018), previously shown to be applicable for both the edges of circular planar sheets and the rupture of surface bubbles, with the present case of aerodynamic droplet breakup. In this theory, the thickness of the receding rim, b, is given, universally, by the criterion $Bo = \rho_l b^2 a / \sigma = 1$. The acceleration used for the case of the surface bubble (i.e. a spherical cap) is taken as the centripetal acceleration:

$$a_c = \frac{u_{rr}^2}{R}, \qquad (4.2)$$

where R is the radius of the bubble. For the present case of the bag, R is approximated by the bag size in the streamwise direction. The receding rim thickness is thus found, by
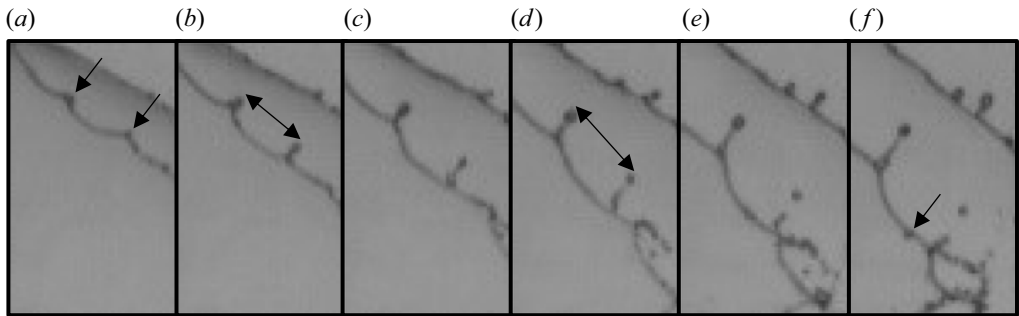
Figure 14. Nascent nodes on receding rim of a breaking water droplet. First, the primary nodes (*a*) form and (*b*) digitate. As the nodes move apart (*c–e*), they open up new space for a nascent node to form on the receding rim (*f*). The initial droplet has diameter $d_0 = 2.08$ mm at $We = 12.2$. The first panel is at $T = 2.18$ (6.95 ms) and the time separation between the panels is $\Delta T = 0.016$ (0.05 ms). See supplementary movie 2.

rearranging $Bo = 1$, as

$$b = \sqrt{\frac{\sigma}{\rho_l a_c}}. \tag{4.3}$$

The receding rim, having thickness b, is then unstable to the Rayleigh–Plateau instability, as

$$\lambda_{RP} = 4.5b. \tag{4.4}$$

An important distinction in this model is that the centripetal acceleration sets the thickness of the receding rim but does not govern its instability. Several other theories have been proposed for the instability of the receding rim; however, we have found that the theory of Wang *et al.* (2018) best matches the present results. An overview and comparison of several theories for the instability of receding rims are given in Appendix C.

When comparing instantaneous measurements of the receding rim wavelength, it is necessary to consider that the rim's geometry is changing in time; mainly, that the rim is expanding. As a result, the nodes may be measured to be farther apart than the estimated wavelength. However, since the rim is assumed to have a constant thickness, it will also continue to be unstable in the same sense throughout its expansion, allowing new nodes to form when the separation between two existing nodes approaches 2λ. This establishes an upper limit on the measurement as 2λ. The phenomenon of the nascent node is shown in figure 14. The nodes on the receding rim first form in figure 14(*a*) and begin to digitate in figure 14(*b*). In figure 14(*c*,*d*), the nodes move apart owing to the expansion of the receding rim. By figure 14(*e*), the nodes are far enough apart for a new node to form on the rim. In figure 14(*f*), the nascent node is clearly visible.

To predict the wavelength based only on the initial droplet conditions, the minimum bag thickness, h_{min}, and the bag radius, R, must be determined.

As mentioned in § 4.1, the mean measured minimum bag thickness is $\bar{h}_{min} = 2.3 \pm 1.2$ μm, and it is proposed that this is indicative of a universal minimum bag thickness for aerodynamic droplet breakup for water. Since the mechanism that leads to this minimum thickness is not known, the effect of viscosity cannot be determined without further investigation. Based on studies of the lifetime of surface bubbles (Poulain *et al.* 2018), one can theorize that the minimum thickness could be either larger or smaller with higher viscosity. On the one hand, the stabilizing effect of higher viscosity has been shown to increase the lifetime of surface bubbles, which may permit more stretching and thus a thinner sheet. On the other hand, higher viscosity also impedes drainage in surface

bubbles, leading to a thicker sheet (which is ultimately one of the stabilizing effects mentioned previously). It should also be noted that a higher viscosity will tend to stabilize the receding rim, and could possibly impede it from corrugating as described here.

The bag radius at burst, R, used to calculate the centripetal acceleration can be estimated based on the semi-analytical bag growth model of Jackiw & Ashgriz (2021). This model is based on a force balance between the thinning bag and the stagnation point flow at its centre, where the breakup point is predicted using the Rayleigh–Taylor piercing criterion of Vledouts *et al.* (2016). From the analysis, Jackiw & Ashgriz (2021) find the bag size, β, as

$$
\frac{\beta(t^*)}{d_0} = \frac{3}{4} \left(\frac{V_0}{V_b} \right) \frac{1}{\tau^2} \left\{ \left[\left(\frac{2R_i}{d_0} \right) - 2 \left(\frac{h_i}{d_0} \right) \right]^2 \frac{t^{*2}}{2} \right.
$$
$$
\left. + \left(\frac{2\dot{R}}{d_0} \right) \left[\left(\frac{2R_i}{d_0} \right) - 2 \left(\frac{h_i}{d_0} \right) \right] \frac{t^{*3}}{3} + \left(\frac{2\dot{R}}{d_0} \right)^2 \frac{t^{*4}}{12} \right\}, \qquad (4.5)
$$

where h_i and d_i are given by (3.6) and (3.8), respectively, and the bag volume V_b/V_0 is estimated as

$$
\frac{V_b}{V_0} = \frac{3}{2} \left[\left(\frac{2R_i}{d_0} \right)^2 \left(\frac{h_i}{d_0} \right) - \left(\frac{2R_i}{d_0} \right) \left(\frac{h_i}{d_0} \right)^2 \left(2 + \frac{\pi}{2} \right) + \pi \left(\frac{h_i}{d_0} \right)^3 \right]. \qquad (4.6)
$$

Equation (4.5) is evaluated at the burst time, t_b^*:

$$
t_b^* = \frac{\left[\left(\frac{2R_i}{d_0} \right) - 2 \left(\frac{h_i}{d_0} \right) \right]}{\left(\frac{2\dot{R}}{d_0} \right)} \left[-1 + \sqrt{1 + C \frac{8\tau}{\sqrt{3We}} \sqrt{\frac{V_b}{V_0}} \frac{\left(\frac{2\dot{R}}{d_0} \right)}{\left[\left(\frac{2R_i}{d_0} \right) - 2 \left(\frac{h_i}{d_0} \right) \right]}} \right], \qquad (4.7)
$$

to find the bag size at burst used in the present analysis for the final radius of the bag, $R_f = \beta(t^*)$. The value of C is determined to be 9.4, considering the modifications made in the present analysis to the prediction of $2R_i$ (see Appendix A). While this model neglects the flow of mass from the interior of the windward disk into the rim described in § 3.2.2, Jackiw & Ashgriz (2021) find that it is sufficient in predicting the size of the bag at burst. This model for R_f is sufficient for $We < 80$ where the bag grows in the downstream direction. However, for $We > 80$ where the bag periphery is dragged downstream, a value of $R_f = R_i$ may be more suitable, as the bag rim does not significantly increase in diameter after initiation.

The model of Wang *et al.* (2018) ((4.4) given (4.3)) using the empirical value of $\bar{h}_{min} = 2.3 \pm 1.2$ μm and the semi-analytical model $R_f = \beta(t^*)$ ((4.5) given (4.7)) is compared with the present measurements in figure 15, where the solid line gives the model prediction given the mean value $\bar{h}_{min} = 2.3$ μm and the grey area gives the limits owing to the standard deviation of ± 1.2 μm. The dashed line gives the upper limit of 2λ, owing to the nascent nodes on the expanding rim.

The results of figure 15 indicate that the model of Wang *et al.* (2018) ((4.4) given (4.3)), using the presently determined empirical value of $\bar{h}_{min} = 2.3 \pm 1.2$ μm and the semi-analytical model $\beta(t_b^*) = R$ (equation (4.5); Jackiw & Ashgriz 2021) gives a good prediction of the receding rim wavelength. Notably, the variation in the minimum bag thickness appears to account almost exactly for the variation in the measured wavelength
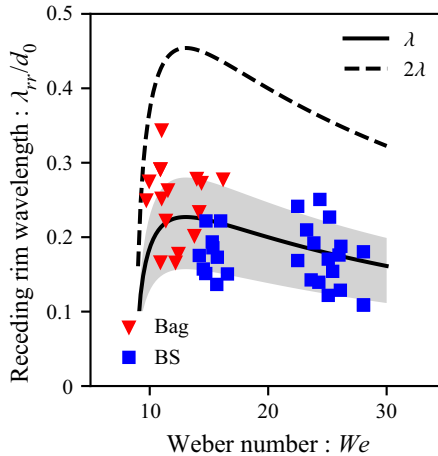
Figure 15. Comparison of the measured receding rim wavelength with the model of Wang *et al.* (2018) ((4.4) given (4.3)) using the empirical value of $\bar{h}_{min} = 2.3 \pm 1.2$ µm and the semi-analytical model $\beta(t_b^*) = R$ (equation (4.5); Jackiw & Ashgriz 2021) with the present measurements. The solid line gives the model prediction given the mean value $\bar{h}_{min} = 2.3$ µm, while the grey area gives the limits owing to the standard deviation of ± 1.2 µm. The dashed line gives the upper limit of 2λ, owing to the nascent nodes on the expanding rim.

on the receding rim. This suggests that variations in the receding rim wavelength are the direct consequence of variations in the minimum bag thickness. Additionally, all measured values are well below the upper limit of 2λ, predicted by the birth of new nodes on the expanding rim, with the exception of low *We*. Since the bag is the largest and has the fewest ruptures at low *We*, the recession time at low *We* is the longest. Thus, the receding rim wavelength is most likely to expand towards the limit of 2λ at low *We*, which matches the results.

4.3. *Liquid sheet breakup*

Although the fragments resulting from the breakup of the liquid sheet are too small to accurately size from the present images ($O(\mu m)$), it is instructive at this time to discuss the mechanisms of their breakup in the context of the bag dynamics described above. In § 6, the relationships discussed here will be compared with data that include sizes from the breakup of the bags.

As with the rupture of surface bubbles, the fragments from the bag come from two phenomena: the fingering of the receding rim (Lhuissier & Villermaux 2012; Wang & Bourouiba 2021) and the collision of two receding rims (Néel, Lhuissier & Villermaux 2020), as shown in figure 16. For both scenarios, previous studies suggest that the droplets from the breakup of the sheet will lie in a range spanning between the sheet thickness, h, and the Rayleigh–Plateau breakup size of the receding rim, $1.89b$, with the added potential for satellite droplets forming from the breakup of both cases. Satellite droplets are discussed further in § 5. This range agrees with the order of magnitude of the droplets observed in the present experiments.

5. Rim breakup mechanisms

The main rim of the droplet is one of the most important geometries in aerodynamic droplet breakup as it contains a majority of the droplet volume (Jackiw & Ashgriz 2021).
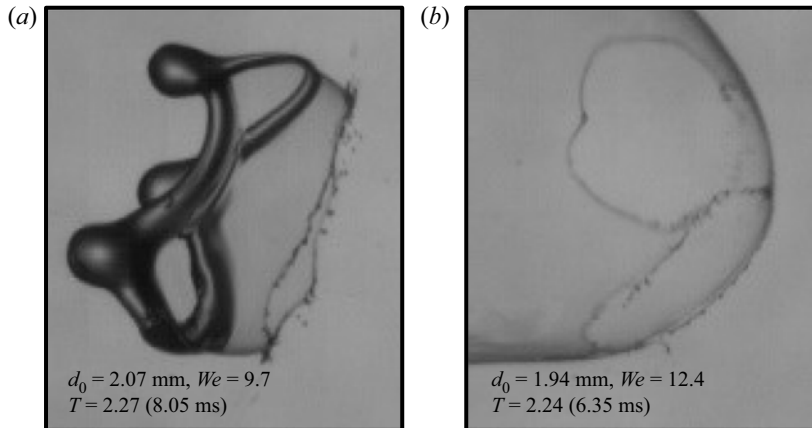
Figure 16. Images of the two dominant bag breakup mechanisms for a water droplet: (*a*) the digitation of receding rim and (*b*) the collision of receding rims.

In previous studies, the rim has been assumed to break via the Rayleigh–Plateau capillary mechanism (Chou *et al.* 1997; Zhao *et al.* 2011; Jackiw & Ashgriz 2021; Obenauf & Sojka 2021), based on its final thickness (minor diameter), as (Ashgriz 2011)

$$\frac{d_r}{d_0} = 1.89 \frac{h_f}{d_0}. \tag{5.1}$$

This theory is derived assuming an axially symmetric liquid column subject to a broad-spectrum, infinitesimal disturbance (i.e. all possible disturbance wavelengths have the same initial amplitude). However, this theory ignores the complication of the effect of the bag on the rim's stability. Furthermore, in our previous study (Jackiw & Ashgriz 2021), we found that the Rayleigh–Plateau breakup mechanism (equation (5.1)) over-predicts the breakup sizes of the rim. Furthermore, it was observed that the rim does not fragment until the bag has fully recessed, suggesting that the rim's stability is affected by the bag. This stabilization effect may manifest in two ways: the stabilization of the rim by the presence of the bag, which modifies the axially symmetric constraint, and the destabilization of the rim induced by the collision of the receding rim, which modifies the initial disturbance. This section aims to identify the mechanisms that couple the rim and bag dynamics and breakup with the goal of obtaining a more realistic prediction of the rim breakup sizes.

Since a more complex curvature is imposed on the rim where it meets the bag, the presence of the bag has a stabilizing effect on the rim. This phenomenon was studied numerically by Bostwick & Steen (2010), who considered the stabilization effect of a rigid wire in contact with the surface of a liquid column or torus. In their work, Bostwick & Steen (2010) found that, in general, the rigid wire constraint tends to stabilize the capillary instability of a liquid column by deforming it into a teardrop shape, as illustrated in figure 17. This shape change modifies the surface curvature such that the surface tension does not act symmetrically about the column's axis, impeding the instability from pinching radially inwards near the tail of the tear droplet. Consequently, the growth rate decreases, and the column's lifetime is increased.

Although the case of the liquid sheet suspended behind the rim does not necessarily impose a rigid wire-like constraint on the rim, the curvature of the rim is modified in a similar way and likely has the same effect on the rim's stability. The stabilizing effect will cease when the bag has fully recessed, allowing the rim to destabilize by the conventional
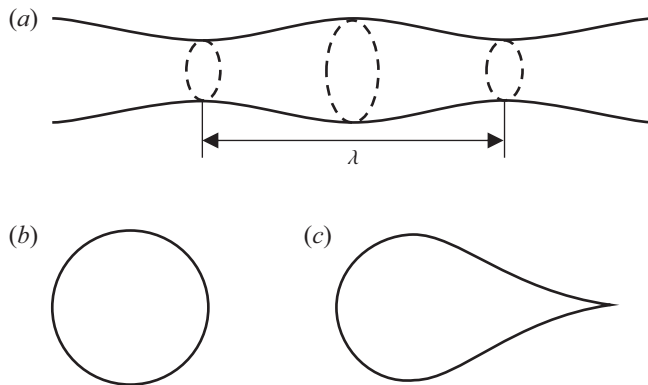
Figure 17. Illustration of (*a*) rim instability, (*b*) idealized rim cross-section without effect of liquid sheet and (*c*) rim cross-section with liquid sheet pulling its side into a teardrop shape, stabilizing it to instability.
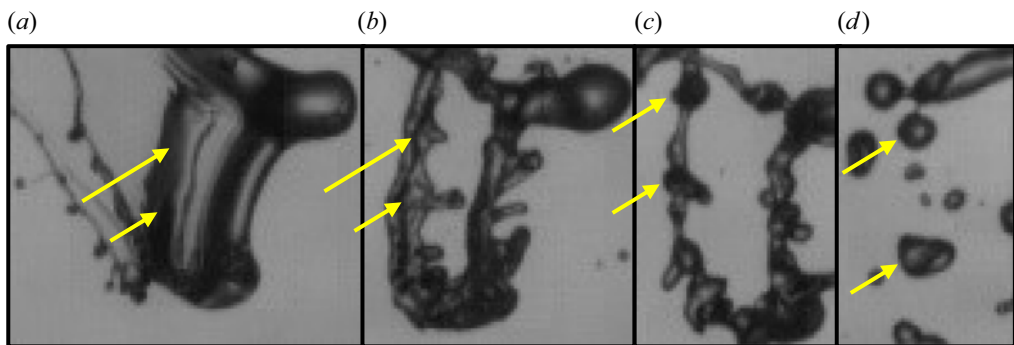

Figure 18. Images of the receding rim colliding with the main rim of the deformed droplet for a breaking water droplet. Arrows highlight the trajectories of two nodes on the receding rim throughout their collision with the main rim, denoting how each results in a distinct droplet from the breakup of the rim. Note that these images are flipped horizontally compared with the other images in this work (i.e. airflow is from right to left) to clarify the bag recession (left to right). The droplet initial conditions are $d_0 = 2.07$ mm and $We = 10.9$. The times are (*a*) $T = 2.33$ (7.8 ms), (*b*) $T = 2.50$ (8.35 ms), (*c*) $T = 2.74$ (9.15 ms) and (*d*) $T = 2.96$ (9.90 ms). See supplementary movie 3.

Rayleigh–Plateau instability (equation (5.1)), rather than at the longer wavelength that would result from the prior stabilization.

While the stabilizing effect of the bag on the rim explains why the rim does not break prior to the completion of the bag recession, it does not account for the over-prediction in the child droplet size of the Rayleigh–Plateau mechanism found in Jackiw & Ashgriz (2021). Here, we propose an alternative mechanism whereby the collision of the receding rim forces the breakup of the main rim.

The dynamics of the collision of the receding rim and the main rim is fundamentally different from that of the collision of two receding rims studied by Néel *et al.* (2020). Since the main rim is considerably larger than the receding rim (by about an order of magnitude), the collision is not symmetric, i.e. the rims are not affected equally by the collision. As a result, the formation of a lamella normal to the collision axis is not observed. In general, the receding rim is absorbed by the main rim when they collide. However, the absorption of the receding rim by the main rim imparts a significant disturbance on the rim. Images of the collision are shown in figure 18.
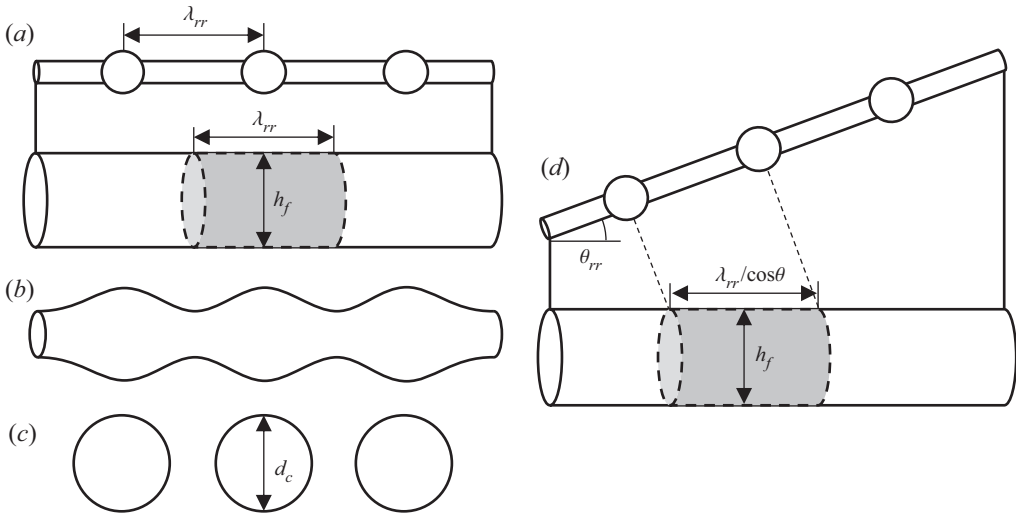
940 A17-26

Figure 19. Illustration of the receding rim collision breakup mechanism geometries. (*a*) Pre-collision, the receding rim corrugated with wavelength λ_{rr} travels towards the main rim of the droplet with thickness h_f. The grey area denotes the rim section that becomes a child droplet after the collision. (*b*) Post-collision, the rim is unstable. (*c*) The rim breaks into droplets of size d_c. (*d*) In the oblique receding rim collision, the receding rim travels at an angle θ_{rr} towards the main rim.

Since the receding rim is heavily corrugated when it collides with the main rim, i.e. the fingering instability discussed in § 4.2, it imparts an unequally distributed force and mass transfer to the rim of the droplet. The nodes or fingers of the rim, having a greater mass than the antinodes, impart a greater force and mass transfer to the main rim than the antinodes. As a result, the receding rim essentially imparts a strong disturbance of wavelength λ_{rr} on the main rim. This disturbance goes on to dominate the rim's breakup, forcing it to occur faster than predicted by the Rayleigh–Plateau theory, and at a dominant wavelength equal to the forced wavelength, λ_{rr}. The resulting droplets will then come from a rim segment of diameter h_f and length λ_{rr}, as

$$\frac{d_r}{d_0} = \left[\frac{3}{2} \left(\frac{h_f}{d_0} \right)^2 \frac{\lambda_{rr}}{d_0} \right]^{1/3}. \tag{5.2}$$

An idealization of the rim collision and its geometries are illustrated in figure 19(*a–c*).

Figures 20(*a*) and 20(*b*) compare the Rayleigh–Plateau (equation (5.1)) and collision (equation (5.2)) models, respectively, with the mean rim breakup size. The present rim collision theory (Collision theo.) is found to match the experiments well while the Rayleigh–Plateau theory (RP theo.) is found to over-predict the breakup sizes.

Since the sheet recesses radially from its initial perforation, not all of the rim collides head-on with the rim. Some of the receding rim will be angled to the axis of the main rim, as illustrated in figure 19(*d*). The recession angle, θ_{rr}, between the receding rim and the main rim will affect the effective wavelength forced on the rim by the collision. Equation (5.2) is then modified by the collision angle as

$$\frac{d_r}{d_0} = \left[\frac{3}{2} \left(\frac{h_f}{d_0} \right)^2 \frac{\lambda_{rr}}{d_0 \cos \theta_{rr}} \right]^{1/3}. \tag{5.3}$$
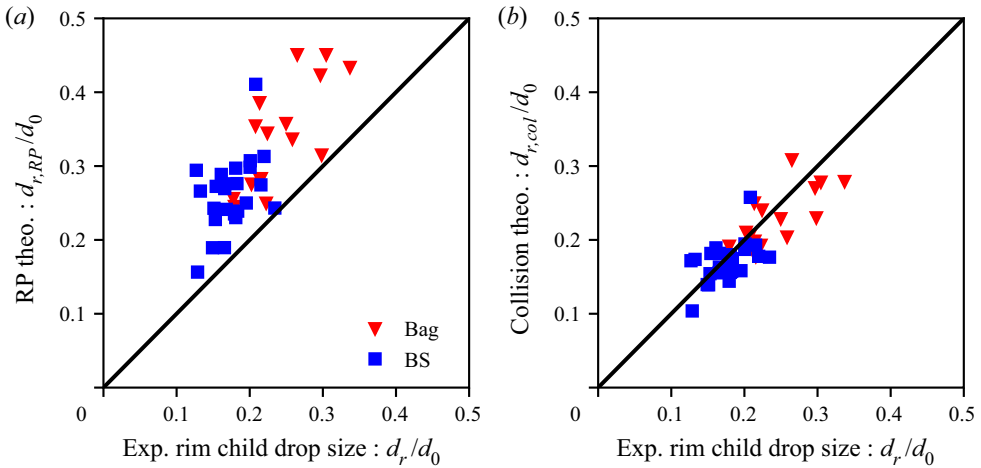
Figure 20. Comparison of (*a*) Rayleigh–Plateau (equation (5.1)) and (*b*) collision (equation (5.2)) breakup mechanism theories with the mean experimental measurements of the rim breakup size.

As θ_{rr} increases, so does the imposed disturbance wavelength; however, the strength of the disturbance decreases. In its limit ($\theta_{rr} = 90°$), the sheet will recess in a direction parallel to the main rim, and no collision will occur. In this case, the collision mechanism will not dominate the breakup, allowing for the Rayleigh–Plateau mechanism to dominate. Notably, this description of the breakup allows for a phenomenological explanation for the distribution of sizes that results from the breakup of the rim, where the width of the distribution comes from the upper and lower limits of the collision angle; namely, the Rayleigh–Plateau (upper) and the head-on collision (lower) mechanisms, where the sizes in between result from the variation in the collision angle.

The last mechanism at play in the breakup of the main rim is the formation of satellite droplets, which result from nonlinearity in the instability of liquid ligaments near the pinch-off point. This dynamics can occur for both the collision and Rayleigh–Plateau breakup mechanisms; however, the smallest sizes of the rim will come from the satellite droplets formed during breakup via the collision mechanism. Keshavarz *et al.* (2020) provide a simple relationship for predicting the satellite droplet sizes as

$$d_s = d_r \frac{1}{\sqrt{2 + 3Oh_r/\sqrt{2}}}, \tag{5.4}$$

where Oh is the Ohnesorge number given by $Oh_r = \mu_l/\sqrt{\rho_l h_f^3 \sigma}$. This relationship is based on an estimation of the thickness of the filament that is formed and stretched in the necking region between two wave crests in Rayleigh–Plateau breakup. Since $Oh_r \ll 1$ for the case of the main rim of the deformed droplet, $d_s \approx d_r/\sqrt{2}$. It is shown in § 5.2 that this prediction follows the lower limit of the spread of the rim breakup sizes, as expected.

Note that satellite formation may also occur in the breakup of the bag, as discussed in § 4.1, where Oh will be based on the receding rim thickness, b, which is much smaller than h_f. As a result, the viscous term is important for the satellite formation in the breakup of the bag.

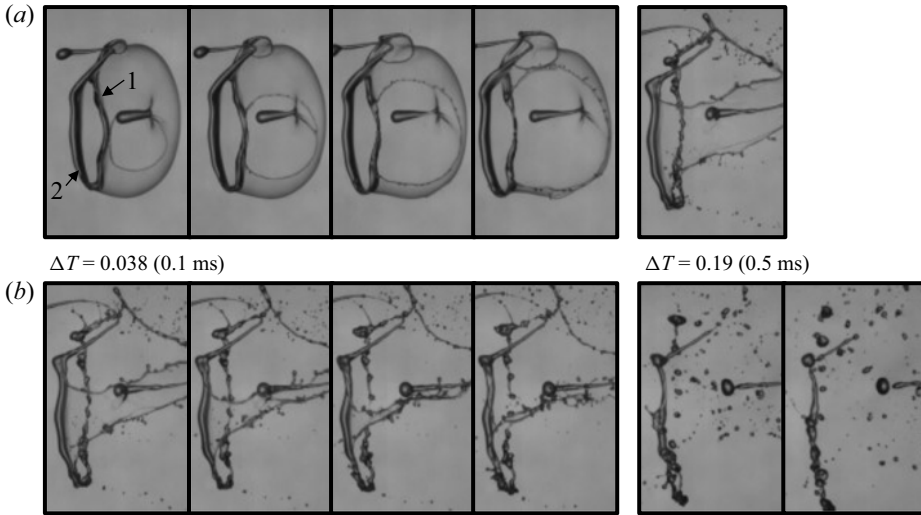$\Delta T = 0.038$ (0.1 ms) $\Delta T = 0.19$ (0.5 ms)

Figure 21. Comparison of breakup by (*a*) the collision mechanism and (*b*) the Rayleigh–Plateau instability for a water droplet. Note that the separated panels on the right are at a larger time interval than those on the left ($\Delta T = 0.038$ (0.1 ms) versus $\Delta T = 0.19$ (0.5 ms)). The initial droplet conditions are $d_0 = 2.02$ mm and $We = 16.6$. The start times of each panel are (*a*) $T = 2.05$ (5.35 ms) and (*b*) $T = 2.39$ (6.25 ms). See supplementary movie 4.

Side	h_f (mm)	t_b (ms)	$t_{b,RP}$ (ms) (equation (5.5))	$t_b/t_{b,RP}$
1	0.30	1.05	8.33	0.13
2	0.26	2.9	6.61	0.44

Table 2. Comparison of measured breakup times of the two sides of the rim with the theoretical breakup time due to the Rayleigh–Taylor instability. The initial droplet conditions are $d_0 = 2.02$ mm and $We = 16.6$.

5.1. *Comparison of rim breakup mechanisms*

As described in the previous section, in some cases the local angle of recession, θ_{rr}, can be so great that the collision is insufficient to dominate the breakup of the rim. In these scenarios, both the collision and Raleigh–Plateau mechanisms can simultaneously dominate the breakup in different regions of the rim. This is exemplified in figure 21, where two sides of the rim appear to be affected by each mechanism independently. In figure 21(*a*), side 1 experiences a direct collision from the receding rim, leading to its breakup. In contrast, in figure 21(*b*), θ_{rr} is very large and the receding rim travels parallel to side 2 such that they do not collide. As a result, the disturbance imparted to side 2 is not as significant as that imparted to side 1. Note that due to irregularities in the rim thickness, the rim thickness of each side is different, as shown in table 2.

The first indication that these mechanisms affect the breakup independently is the difference in the breakup time of each side. Table 2 gives the measured breakup times of sides 1 and 2 as well as the predicted breakup time of the Rayleigh–Plateau theory (Ashgriz 2011),

$$t_{b,RP} = \frac{13}{0.97\sqrt{\dfrac{\sigma}{\rho_l h_f^3}}}, \tag{5.5}$$

Side	$\bar{d}_r$ (mm)	$d_{r,coll}$ (mm) (equation (5.2))	$d_{r,RP}$ (mm) (equation (5.1))	$\bar{d}_r/d_{r,coll}$	$\bar{d}_r/d_{r,RP}$
1	0.38	0.35	0.57	1.08	0.65
2	0.48	0.31	0.49	1.53	0.97

Table 3. Comparison of measured breakup sizes of the two sides of the rim with the theoretical breakup sizes predicted by the collision (equation (5.2)) and Rayleigh–Plateau instability (equation (5.1)) breakup mechanisms. The initial droplet conditions are $d_0 = 2.02$ mm and $We = 16.6$.

and the ratio between the measured and predicted breakup times. From table 2, the measured breakup time of side 2 is three times that of side 1, which can be seen in figure 21 where side 2 (figure 21*b*) remains stable for much longer than side 1 (figure 21*a*) after the sheet has fully recessed. Notably, the measured breakup time of side 1 is less than that of side 2 despite side 1 being thicker than side 2, which would otherwise tend to increase the breakup time as predicted by the Rayleigh–Plateau theory. This observation emphasizes the effect of the collision mechanism where the strong addition of a specific disturbance significantly decreases the breakup time of the rim. These findings are consistent with the present theory that the impact of the corrugated rim accelerates the breakup of the main rim.

The mean child droplet sizes, $\bar{d}_r$, from each side of the rim as well as the predictions of the present collision theory (equation (5.2)) and the Rayleigh–Plateau breakup theory (equation (5.1)) along with comparisons of each with $\bar{d}_r$ are given in table 3. The results of table 3 indicate that the breakup sizes of side 1 are most accurately predicted by the present collision theory, while those of side 2 are most accurately predicted by the Rayleigh–Plateau theory.

The results of both breakup time and size for the two sides of the rim shown in the present case provide strong evidence for the existence and validity of the proposed receding rim collision breakup mechanism. Furthermore, the results show how both mechanisms can occur in the same breakup event, which contributes to a wider distribution of sizes generated by the breakup.

Note that while the predicted breakup time of side 2 (the Rayleigh–Plateau case) is also larger than that measured, this is likely due to the additional disturbance imparted to the rim by the collision of the receding rim, which would result in a lower breakup time than predicted by (5.5); however, in this case, the additional disturbance only decreases the breakup time and does not significantly affect the wavelength that breaks the rim. This is evidenced by the breakup sizes from the rim.

5.2. *Summary of rim breakup*

Having a view of the various mechanisms of rim breakup, we can now give an overview of how the variation in mechanism results in the distribution of sizes that result from the breakup of the rim, which are shown in figure 22.

Firstly, the largest sizes in the rim's breakup result from the Rayleigh–Plateau mechanism. The prediction of (5.1) matches well the upper limit of the sizes in the present experiments in terms of both magnitude and trend, as shown in figure 22.

The majority of the breakup sizes result from the present collision mechanism, which well describes the mean size of the droplets. Two fundamental factors influence the collision mechanism sizes: the minimum bag thickness, h_{min}, which affects the receding
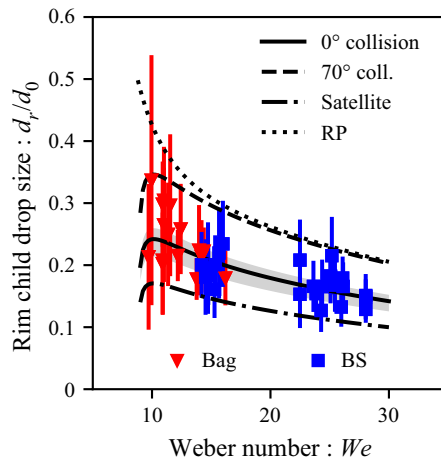
Figure 22. Range of rim child droplet sizes compared with the collision (with satellite droplets) and Rayleigh–Plateau mechanisms. The vertical lines denote the standard deviation of the measured rim droplet sizes for each case to show their spread. The grey area gives the range of the collision mechanism considering the standard deviation in the bag thickness (see § 4).

rim instability, and the collision angle, θ_{rr}, which affects the effective imposed wavelength. As discussed in § 4, h_{min} is approximately constant for all present cases, as $h_{min} = 2.3 \pm 1.2$ µm, giving a small variation to the collision mechanism about the mean. This is denoted by the grey area in figure 22. The collision mechanism has the tendency to increase the breakup size as θ_{rr} increases.

The smallest sizes of the breakup come from the satellite droplets (equation (5.4)) that form from the head-on collision of the receding rim. Note that satellite droplets may also form from the oblique collision of the receding rim, as well as from the Rayleigh–Plateau rim breakup mechanism. These satellites will be larger than those from the head-on collision, and thus fill out the distribution of sizes between the smallest satellites and the primary breakup mechanisms.

6. Prediction of the droplet size distribution

In the previous sections, predictions have been laid out for the mean, minimum and maximum expected droplet sizes from a variety of breakup mechanisms. These mechanisms together result in the distribution of sizes from aerodynamic droplet breakup; however, in order to predict the distribution, one must know the relative contribution of each breakup mechanism as well as how the variation of each mechanism is distributed about its mean. While the relative contributions of the main breakup modes (rim nodes, remaining rim and bag) can be estimated from the droplet geometry predictions, the problem of identifying the relative contributions of the individual mechanisms to each mode quickly becomes intractable due to the large number of unknowns. It is therefore convenient to lump the mechanisms within each main mode together and approximate their relative contribution to each mode by assuming a distribution function. The overall distribution will then consist of the weighted sum of the distributions for each mode of the breakup.

Previous works on ligament breakup have empirically fitted the single-parameter gamma distribution function to data for the fragmentation of a corrugated ligament (Marmottant & Villermaux 2004; Villermaux *et al.* 2004) and for the analogous case of the rim in

aerodynamic droplet breakup (Villermaux & Bossa 2009; Zhao *et al.* 2011). In these works, the gamma distribution was assumed to be related to the distribution in the corrugation of the ligament, which is susceptible to the capillary instability, rather than to the summation of a variety of breakup mechanisms. In this sense, these works assume that the variation in the sizes comes from the corrugation of the ligament or rim. Although this may be appropriate for the fragmentation of corrugated ligaments, the presence of multiple breakup mechanisms in aerodynamic droplet breakup as presented in the present work makes this assumption questionable for the fragmentation of the structures formed in aerodynamic droplet breakup. Furthermore, no works to date have provided either an analytical prediction of the distribution parameters or a prediction of the combined multimodal distribution for aerodynamic droplet breakup. In this section, we propose a methodology for estimating the distribution parameters based on the analytical predictions of the characteristic sizes that result from the many mechanisms that contribute to the breakup developed in the preceding sections.

Since the present experiments do not provide a complete view of the distribution of the breakup sizes as a result of insufficient resolution for the bag breakup sizes and only single instances of breakup captured for each *We* case, we choose to compare our analysis with the results of Guildenbecher *et al.* (2017). The distribution data of Guildenbecher *et al.* (2017) were gathered using the digital in-line holography technique, which resolved sizes down to 27 µm, and are based on the accumulation of 42 instances of ethanol ($\rho_l = 789 \text{ kg m}^{-3}$, $\mu_l = 1.2 \text{ mPa s}$ and $\sigma = 2.44 \text{ mN m}^{-1}$) droplet breakup at both low *We* (13.8, $d_0 = 2.54$) and high *We* (55.3, $d_0 = 2.55$). Note that Guildenbecher *et al.* (2017) showed (using a high-magnification set-up) that droplets below 27 µm exist in the spray for the low-*We* case; however, they are omitted in the present case for consistency between the low- and high-*We* cases.

6.1. *Modelling of the breakup distributions*

Following the previous works, it is assumed that the number of droplets formed by the mechanisms within each mode are related approximately by a two-parameter gamma probability density function, giving the number probability density function, p_n, as

$$p_n(x = d/d_0; \alpha, \beta) = \frac{x^{\alpha-1} \, e^{-x/\beta}}{\beta^\alpha \, \Gamma(\alpha)}, \tag{6.1}$$

where $x = d/d_0$ are the droplet sizes, Γ is the gamma function, α is the shape parameter and β is the rate parameter. Both α and β must be greater than zero. For the two-parameter distribution, α and β can be estimated using the method of moments estimators as

$$\alpha = (\bar{x}/s)^2 \tag{6.2}$$

and

$$\beta = s^2/\bar{x}, \tag{6.3}$$

where $\bar{x}$ and s are the number mean and standard deviation of the distribution, respectively. The estimation of $\bar{x}$ and s from the models presented in the present work is discussed later in this section.

Despite containing much less of the volume of the parent droplet, the smaller modes of breakup dominate p_n and obscure the larger modes as the number of droplets resulting from the breakup mechanisms increases with decreasing child droplet size. It is therefore more helpful to compare the volume-weighted probability density functions, p_v, rather

than p_n, as this allows significantly better visualization of the larger modes. Also, p_v is more useful in most industrial processes as the primary functions of many processes involving sprays depend on how much of the sprayed volume breaks into a certain size range. Function p_v is obtained by weighting p_n by x^3 and renormalizing the distribution:

$$p_v = \frac{x^3 p_n(x)}{\int_0^\infty x^3 p_n(x) \, dx} = \frac{x^3 p_n(x)}{\beta^3 \Gamma(\alpha+3)/\Gamma(\alpha)}. \tag{6.4}$$

The resulting distribution of the breakup will be the weighted sum of all modes of breakup, given by

$$p_{v,Total} = \sum_{i=1}^{\hat{n}} w_i p_{v,i}, \tag{6.5}$$

where w_i is the volume weight of the ith mode of the breakup determined by conservation of volume and $\hat{n}$ is the total number of modes.

The modes that contribute to the breakup of the droplet depend on the breakup morphology. In particular, the existence and mechanisms of breakup of the undeformed core play a significant role in the overall breakup, as the core can contain a considerable volume of the parent droplet and undergoes a separate breakup event that contributes additional modes to the breakup (Jackiw & Ashgriz 2021). The methodology of modelling the multimodal distribution of aerodynamic droplet breakup (i.e. the estimation of w_i for the modes of breakup as well as $\bar{x}$ and s from the models presented in the present work) for the simpler case of the bag breakup morphology is outlined next, followed by the methodology for extending the model to the case of the breakup of the undeformed core in the MB breakup morphology.

6.2. *Prediction of size distribution in bag breakup*

In the case of the bag breakup morphology, no undeformed core is formed during the breakup. Consequently, the only modes that contribute to the breakup sizes in bag breakup are the rim nodes, the remaining rim and the bag sizes. The combined p_v of the nodes, rim and bag is then given by the weighted summation of each mode:

$$p_{v,Total} = w_N p_{v,N} + w_r p_{v,r} + w_b p_{v,b}. \tag{6.6}$$

As discussed in § 3.2.2, the node volume is found as

$$w_N = \frac{V_N}{V_0} = \frac{V_N}{V_d} \frac{V_d}{V_0}, \tag{6.7}$$

where the mean value of $V_N/V_d \approx 0.4$ was determined in § 3.2.2 and V_d/V_0 is given by (3.17).

The volume of the rim,

$$w_r = V_r/V_0, \tag{6.8}$$

is given by (3.16). Note that, as discussed in § 3.4, the rim maintains an approximately constant volume despite the flow from the rim into the nodes owing to the flow into the

rim from the bag. The volume of the bag is then given by the remaining volume as

$$\frac{V_b}{V_0} = 1 - \frac{V_N}{V_0} - \frac{V_r}{V_0}. \tag{6.9}$$

Although the the undeformed core is neglected in this instance, the definition of w_N, w_r and w_b still results in a leftover core volume of $V_c/V_0 \approx 0.05$. Since this volume is neglected when determining the total distribution, the integral will be ≈ 0.95. The justification for omitting this size from the present analysis is discussed later in this section.

As mentioned previously, the distribution parameters α and β can be estimated from $\bar{x}$ and s ((6.2) and (6.3), respectively), which, in turn, are related to the child droplet sizes of the breakup mechanisms presented in the present work.

In the previous sections, the sizes predicted for the mechanisms within each mode were shown to give reasonable estimations of the number-based mean and spread of the present data; however, these limits do not translate directly to the true mean ($\bar{x}$) and standard deviation (s) of the droplet sizes since the weighting of the mechanisms within each mode is not considered. This is evidenced by the distance from the estimated mean to the estimated upper and lower limits being asymmetric. The relative weighting is introduced by enforcing the two-parameter gamma distribution assumption (i.e. assuming that the mechanisms in each mode are weighted such that the mode overall follows a gamma distribution). This is done by assuming that the mean and standard deviation of the distribution are equal to the mean and standard deviation of all of the combined mechanisms (weighted equally) within each mode, which are modelled by discrete predictions. The mean and standard deviation are then given by

$$\bar{x} = \frac{\sum_{i=1}^{\check{n}} x_i}{\check{n}} \tag{6.10}$$

and

$$s = \sqrt{\frac{\sum_{i=1}^{\check{n}} (x_i - \bar{x})}{\check{n}}}, \tag{6.11}$$

where x_i are the characteristic sizes of each mode ($x = d/d_0$) and $\check{n}$ is the total number of characteristic sizes.

The breakup mechanism of the node drops (§ 3) is the simplest of the three breakup modes of bag breakup as there is only one characteristic mechanism, which contains its own inherent variation. The variation in the Rayleigh–Taylor instability theory for the mechanism of the node breakup comes from the variation in the node-wavelength volume fraction, n, which ranges from its lower limit of $n = 0.2$ to an upper limit of $n = 1$ with a typical value of $n = 0.4$. The number-based mean and standard deviation of the node mode are then estimated by taking the mean and standard deviation of the three characteristic sizes that result from each of these three values (i.e. the upper, lower and typical values) in (3.15), weighted equally. The three predicted characteristic breakup sizes of the nodes are compared with the distribution data of Guildenbecher *et al.* (2009) in figure 23(*a*).

The breakup of the rim (§ 5) is somewhat more complex, as it consists of two mechanisms, i.e Rayleigh–Plateau (equation (5.1)) and the receding rim collision (equation (5.2)), as well as the formation of satellite droplets and the inherent variation
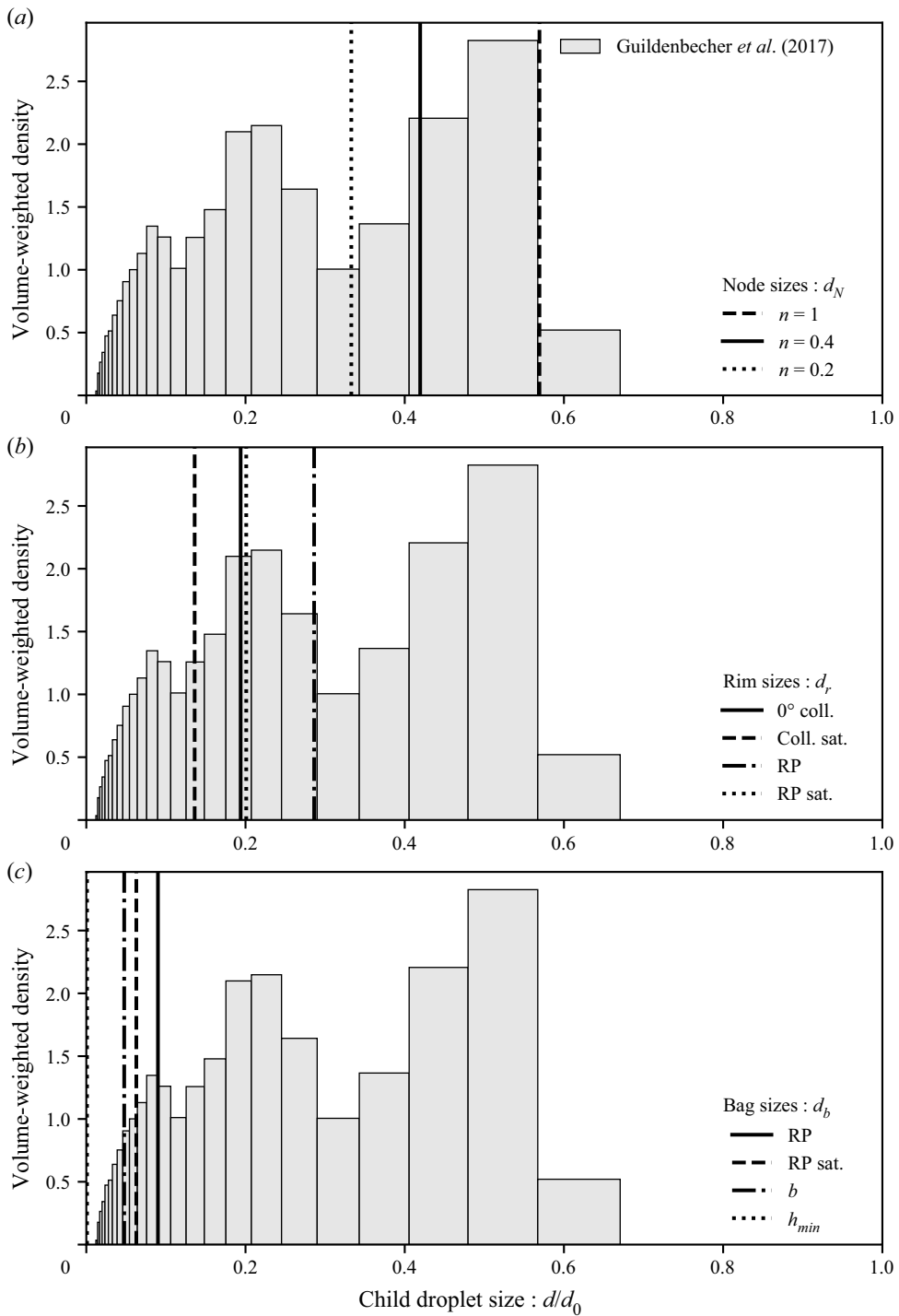
Figure 23. Comparison of the present predictions for the multimodal distribution with measurements from Guildenbecher *et al.* (2017) for ethanol drops of initial diameter $d_0 = 2.54$ mm at $We = 13.8$ for the breakup of (*a*) the nodes, (*b*) the remaining rim and (*c*) the bag.

Mode	α	β	w ((6.7)–(6.9))	w (fit)
Nodes	20	0.022	0.38	0.57
Remaining rim	14.5	0.014	0.45	0.28
Bag	2.4	0.021	0.12	0.15

Table 4. Distribution parameters for the case of ethanol drops of initial diameter $d_0 = 2.54$ mm at $We = 13.8$, corresponding to the experiments of Guildenbecher *et al.* (2017) shown in figure 24.

of each. However, the sensitivity of the mechanisms to their variations is relatively small, and thus it will be assumed that only the primary mechanisms, as well as the satellite droplets, dominate the number distribution. Therefore, the number-based mean and standard deviation for the breakup of the remaining rim are estimated from four sizes, weighted equally: the Rayleigh–Plateau mechanism ($d_{r,RP}$, (5.1)), the receding rim collision mechanism ($d_{r,coll.}$, (5.2), assuming $\theta_{rr} = 0$) and the satellite sizes that result from each ($d_{r,RP\,sat.}$ and $d_{r,coll.\,sat.}$, (5.4)). The four predicted characteristic breakup sizes of the rim are compared with the distribution data of Guildenbecher *et al.* (2009) in figure 23(*b*).

The mechanisms of the bag's breakup (§ 4) are somewhat ill-defined, as the present experiments were unable to capture these sizes. The main mechanism identified in the literature is the Rayleigh–Plateau breakup of the receding rim ($d_{b,RP} = 1.89b$, where b is given by (4.3)), which will also be accompanied by satellite droplets ($d_{b,\,RPsat.}$, given by (5.4)). However, comparing with the data of Guildenbecher *et al.* (2009), the sizes may be much smaller and approach the thickness of the sheet, h_{min}. As such, we suggest that two additional mechanisms of breakup in the bag result in sizes of the order of the sheet thickness, h_{min}, as well as the rim thickness, b. The number-based mean and standard deviation of the bag mode are then estimated by taking the mean and standard deviation of these four characteristic sizes, weighted equally. The four predicted characteristic breakup sizes of the bag are compared with the distribution data of Guildenbecher *et al.* (2009) in figure 23(*c*).

Figure 23(*a*) shows that the largest peak is due to the node drops, where the characteristic sizes are given by $n = 1$, $n = 0.4$ and $n = 0.2$. Figure 23(*b*) shows that the central peak is the result of the breakup of the remaining rim, where the characteristic sizes are given by the collision mechanism, the Rayleigh–Plateau instability and the satellite droplets resulting from both. Figure 23(*c*) shows that the smallest peak is due to the breakup of the bag where the characteristic sizes are given by the Rayleigh–Plateau breakup of the receding rim and its associated satellite droplets as well as the characteristic sizes of the receding rim and bag sheet thickness. For all three modes, the spread of each mode is well captured by the constituent breakup mechanisms.

Having estimated $\bar{x}$ and s from the characteristic breakup mechanisms, α and β can be determined using (6.2) and (6.3), respectively, and thus the combined p_v of the three modes (equation (6.6)) can be predicted. Figure 24(*b*) compares the analytical prediction of the combined distribution with the distribution data of Guildenbecher *et al.* (2009). The distribution parameters determined by the present method are provided in table 4.

From figure 24(*a*), it can be seen that while the location and width of the peaks are reasonably matched by the semi-analytical distribution, the heights of the peaks are not so well predicted. The contribution of the central peak due to the rim breakup is over-predicted, while the left and right peaks, due to the breakup of the bag and nodes, respectively, are under-predicted. One possible explanation for this is that the assumed
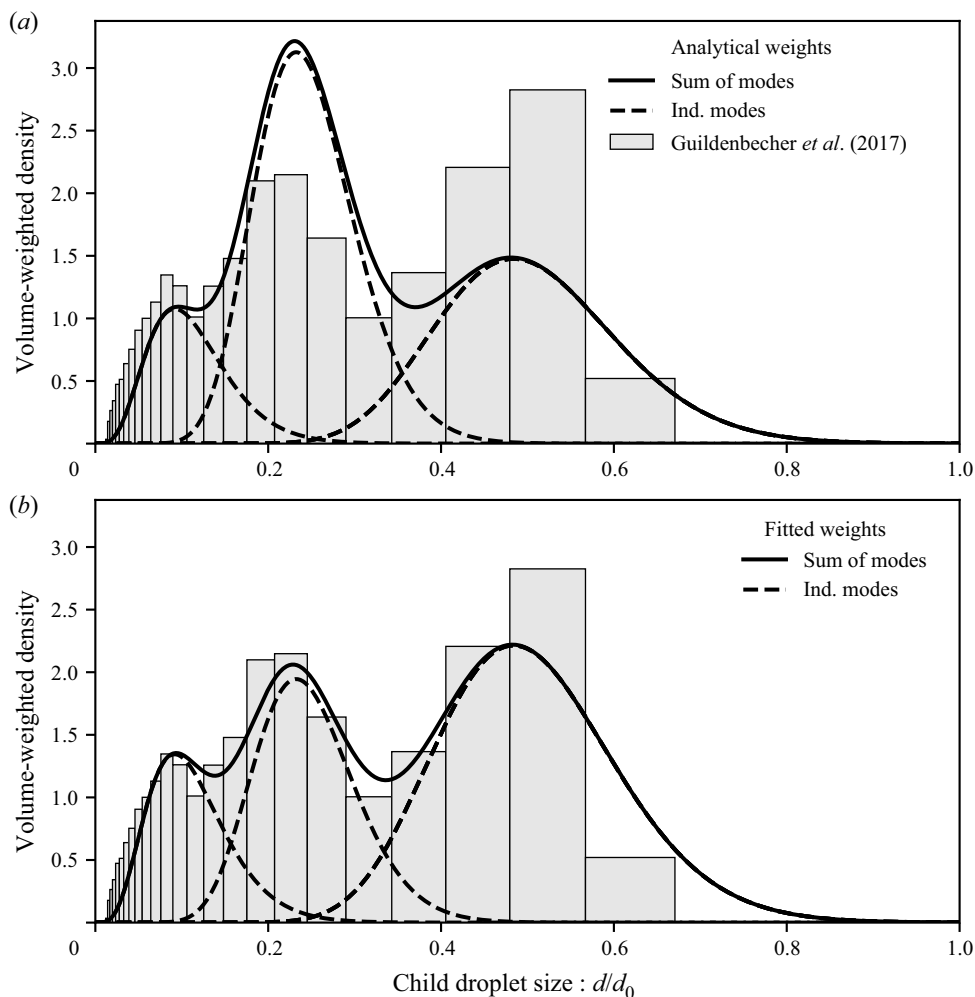
Figure 24. Comparison of the present predictions for the multimodal distribution with measurements from Guildenbecher *et al.* (2017) for ethanol drops of initial diameter $d_0 = 2.54$ mm at $We = 13.8$. (*a*) Distribution predictions using analytical weighting. (*b*) Distribution with best-fit weighting.

distribution weights ((6.7)–(6.9)) do not accurately represent the experiment. The weights used in the present analysis were derived specifically for the bag breakup morphology, while the experiment is near the transition to the BS breakup morphology ($We \approx 15$; Jackiw & Ashgriz 2021). Near this transition, the breakup may exhibit the 'twin-bag' transitional morphology described in Jackiw & Ashgriz (2021), where a fold appears across the bag dividing it in two owing to the slightly larger mass at the centre of the bag due to the small undeformed core, which was neglected in the present analysis as discussed earlier. While this fold primarily affects the bag, it may also have an influence on the rim; in particular, the formation of additional nodes on the rim where it is met by the fold of the bags. The presence of this fold then changes the assumed dynamics of the rim and thus may reduce the remaining rim's volume and thickness more than presently predicted, leading to the over-prediction in the volume contribution of the rim. The fold itself may also contribute additional large sizes to the breakup as it may form

as a ligament that is left behind after the rupture of the bag. The ligament left behind is visible in the digital in-line holography images of Guildenbecher *et al.* (2017), although it is not included in their breakup data, which are used here. This ligament may also be akin to the undeformed core neglected from the present analysis, which contains approximately 5 % of the initial droplet's volume corresponding to a size of $d/d_0 \approx 0.38$. Furthermore, it may be that several of the experimental cases led to the formation of a small stamen that additionally contributes to the volume in the large mode. Another explanation for why the remaining rim volume weight is over-predicted is that the dynamics of the node formation varying at low *We* is not fully captured. If the flow from the bag to the rim is insufficient to match the flow from the rim to the nodes (i.e. $m < n$ in (3.18); see § 3.4 and figure 8) then the volume contribution of the remaining rim will be lower while that of the nodes will be higher. This is the case at very low *We* (*We* < 11) where the present model gives a non-physical prediction for the bag volume of $w_b < 0$ due to the over-prediction of the remaining rim volume, w_r. This suggests that there is a limiting factor in the flow from the bag to the rim at very low *We* that is not captured in the present work; however, such an investigation is outside of the present scope.

To see the effect of having a better prediction of the distribution weights, w_N, w_r and w_b are fitted to the experimental data in figure 24(*b*). The fitted weights are given in table 4. Although the combined distribution naturally matches the experimental data better, there are some deviations such as the valleys between the peaks and the right tail of the large mode, which reaches above a value of $d_c/d_0 = 0.78$, giving drops that contain more than half of the initial droplet volume. Notably, in figure 9, although the prediction of the upper limit continues to increase as *We* decreases, the upper bar of the lowest *We* data points does not exceed $d_N/d_0 \approx 0.7$. These discrepancies may be solved by a narrower distribution, which can be obtained by changing either of the gamma distribution parameters, α or β. Due to the nature of the probability density function, the height of the peaks may also be affected by these changes. However, it is important to remember that these distribution parameters are an inherited part of the core assumption of this section: that the relative contribution of each mechanism to the overall mode is approximated by a gamma distribution function. The proposition of altering either of these parameters thus must also include the proposition of selecting a different distribution entirely. In particular, a truncated or bounded distribution may be more appropriate, as some of the mechanisms presented in the present work offer an upper physical bound on the child droplet size that is not captured by a gamma distribution. However, the comparison of different distributions is left out of the scope of the present work.

6.3. *Breakup of the undeformed core*

At higher-*We* droplet breakup, the undeformed core also contributes to the breakup of the parent droplet and may undergo its own multimodal breakup, i.e. the 'core breakup'. Thus, the undeformed core contributes additional modes to the breakup, and must be included in the analysis. The volume of the undeformed core is given by Jackiw & Ashgriz (2021) as

$$w_c = \frac{V_c}{V_0} = 1 - \frac{V_d}{V_0}, \tag{6.12}$$

where V_d/V_0 is given by (3.17). The bag volume is then the volume of the windward disk not contained in the nodes or the remaining rim:

$$w_b = \frac{V_b}{V_0} = \frac{V_d}{V_0} - \frac{V_N}{V_0} - \frac{V_r}{V_0}. \tag{6.13}$$
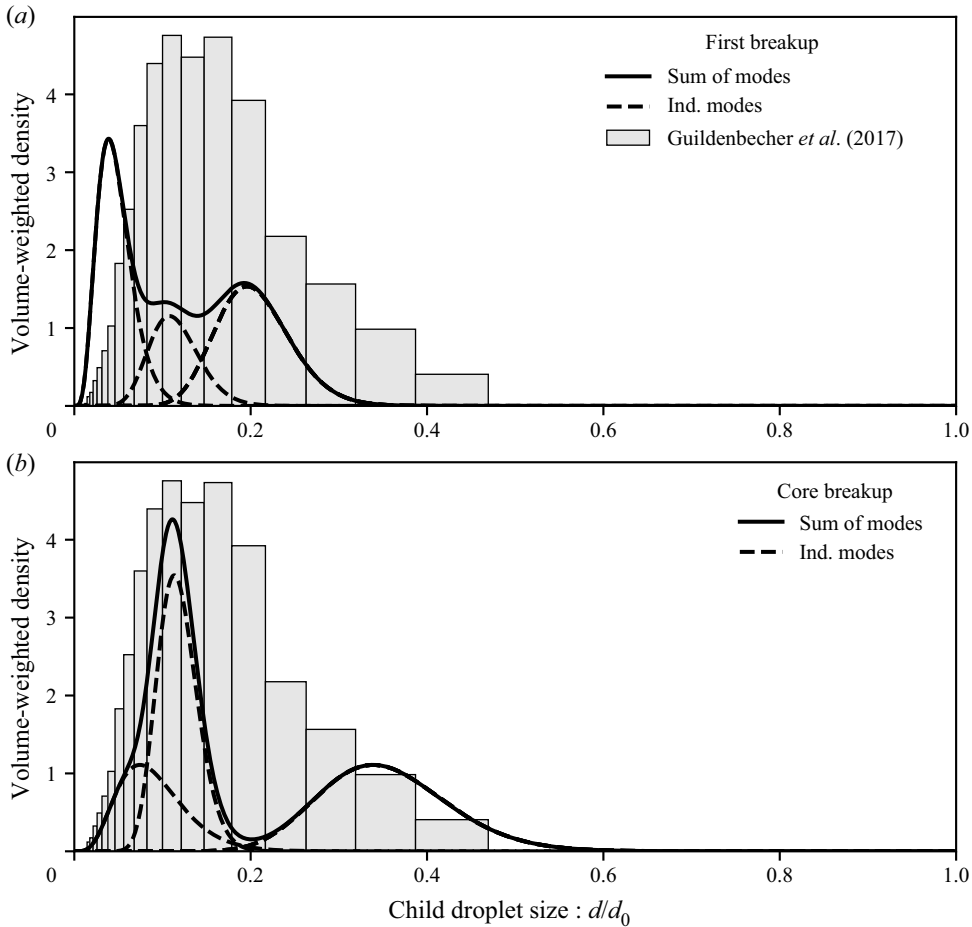
Figure 25. Comparison of present predictions of the (*a*) first and (*b*) core breakup event measurements from Guildenbecher *et al.* (2017) for ethanol drops of initial diameter $d_0 = 2.55$ mm at $We = 55.3$. Note that the distributions in (*a*) and (*b*) are weighted by their volume contributions relative to the parent droplet, and thus their respective integrals are < 1.

The volume contributions of the node and rim modes are calculated as in § 6.2 ((6.7) and (6.8), respectively). The first breakup event, wherein the initial windward disk breaks and leaves the undeformed core behind, is modelled as in § 6.2, while the core breakup is treated separately.

The predicted distribution of the first breakup consisting of the node, rim and bag breakup sizes is compared with the data of Guildenbecher *et al.* (2017) in figure 25(*a*). Note that the plotted distributions are weighted by their respective volume contributions with respect to the parent droplet; thus, their respective integrals are < 1. The distribution parameters and weights are given in table 5.

Figure 25(*a*) shows that the first breakup contributes predominantly to smaller sizes. However, the contributing volume of the bag appears to be over-predicted, especially considering that the first breakup contributes less than half of the total breakup volume in the present case. This is likely due to the folds between the azimuthal bags being neglected. The folds between the azimuthal bags leave behind ligaments after the rupture of the bags, which result in sizes similar to the breakup of the rim. As a result, some of the mass of

Mode	α	β	w ((6.7)–(6.9))
Nodes	20	0.0088	0.16
Remaining rim	13.4	0.007	0.08
Bag	2.5	0.0086	0.16
Core	—	—	0.6
Core nodes	20	0.015	0.2
Core rim	23.5	0.0044	0.2
Core bag	2.4	0.017	0.1
Core nodes	20	0.015	0.2
Nodes + core rim	8.1	0.016	0.36
Rim + bags	1.6	0.029	0.34

Table 5. Distribution parameters for the case of ethanol drops of initial diameter $d_0 = 2.55$ mm at $We = 55.3$, corresponding to the experiments of Guildenbecher *et al.* (2017) shown in figures 25 and 26.

the bag breaks into sizes similar to those of the rim breakup. Since this effect is neglected, the smallest sizes due to the breakup of the bag are over-predicted, while the sizes near the characteristic sizes of the rim breakup are under-predicted.

After the first breakup event, the undeformed core remains, which may also break due to the aerodynamic forces. It is therefore necessary to analyse the breakup of the undeformed core in the same manner as the breakup of the parent droplet; however, assumptions must be made about the aerodynamic conditions of the undeformed core.

The undeformed core is assumed to be represented by an effective droplet size by

$$\frac{d_c}{d_0} = \left(\frac{V_c}{V_0}\right)^{1/3}, \tag{6.14}$$

where V_c/V_0 is given by (6.12). Since the core droplet does not form until after the first breakup event has occurred, the acceleration of the parent droplet must be considered. The speed of the core droplet after the first breakup event, U_c, is found by assuming a constant acceleration due to drag as

$$U_c = \frac{3}{4}\bar{C}_D T_b \left(\frac{2R_i}{d_0}\right)^2 \frac{d_0}{\tau}, \tag{6.15}$$

where T_b is the non-dimensional burst time ($T_b = T_i + T_b^*$, where $T_i \approx 0.9$ (Jackiw & Ashgriz 2021) and T_b^* is computed from (4.7)) and $\bar{C}_D$ is the average drag coefficient over the initiation and bag blow-out given by Chou *et al.* (1997) as 3.33 (calculated from the weighted average of the reported drag coefficients for the initiation and bag blow-out times). Using d_c and the relative velocity $U - U_c$, the conditions of the core droplet, We and τ, can be determined. The breakup model is then repeated until the core droplet does not meet the conditions for breakup ($We \approx 8.8$; Jackiw & Ashgriz 2021). Since the second breakup event constitutes only a portion of the initial parent droplet, the weights of the modes from the core breakup must be adjusted so that they represent the weighting with respect to the parent droplet by multiplying each of the core breakup weights by the core volume weight, w_c.

For the present case, the core droplet properties are found as $d_c = 2.15$ mm, $U_c = 7.8$ m s^{-1} ($U - U_c = 13.2$ m s^{-1}) and $We = 18$. The present prediction of U_c is in reasonable agreement with the speed of the larger child drops measured by Guildenbecher *et al.* (2017) ($U_c \approx 10$ m s^{-1}). The core droplet, therefore, undergoes BS breakup. In this

case, *We* of the core droplet is low enough that a second core breakup event does not occur; however, it is possible that a second core droplet that does not break will remain. The volume of the leftover undeformed core is implicit in the calculation of the weights of the core modes, resulting in a volume deficiency of 0.09 between the total core volume and the volume of the modelled modes. This is the volume of the leftover core droplet, which would have an estimated size of $d_c/d_0 \approx 0.45$. This second core droplet would have $We \approx 2$, and therefore would not break further. Such a droplet is visible in the images of Guildenbecher *et al.* (2017), but is not captured in the measurement with which the present analysis is being compared. For this reason, the second undeformed core is neglected in the present analysis.

The resulting size distribution of the core breakup event is compared with the results of Guildenbecher *et al.* (2017) in figure 25(*b*). As with figure 25(*b*), the plotted distributions are weighted by their respective volume contributions with respect to the parent droplet; thus, their respective integrals are < 1. The distribution parameters and weights are given in table 5. Figure 25(*b*) shows how the core breakup contributes to the larger sizes in the size distribution of the breakup. The combined distribution of the first and core breakup events is compared with the data in figure 26(*a*).

In the combined distribution, the largest sizes come from the nodes of the breakup of the core, while the smallest sizes come from the breakup of the bag in the first breakup event. The remaining modes fill in the intermediate sizes of the distribution, with reasonable agreement between the prediction and the data of Guildenbecher *et al.* (2017) for sizes above $d/d_0 \approx 0.2$. However, the combined distribution suffers the same overestimation of the smallest sizes as the first breakup event as mentioned earlier in this section. With the correction of these factors, the predicted distribution would be expected to match the experimental data much better in this range.

Since the modes of the first nodes and second rim overlap, as well as the modes of the first rim and the first and second bags, it may be convenient to lump these modes together such that the overall breakup consists of only three modes instead of six: the first rim and the first and second bags giving the smallest mode, the first nodes and the second rim giving the intermediate mode and the second nodes giving the largest mode. In doing so, the effect of the folds between the azimuthal bags that results in the misprediction of the bag and rim contributions can be reduced. The distribution parameters of the combined bag and rim mode are then calculated by the weighted mean and standard deviation of the constituent breakup mechanisms of both the bag and rim modes of breakup. The weighted mean, $\bar{x}_w$, and standard deviation, s_w, are calculated as

$$\bar{x}_w = \frac{\displaystyle\sum_{i=1}^{\check{n}} w_i x_i}{\displaystyle\sum_{i=1}^{\check{n}} w_i} \tag{6.16}$$

and

$$s_w = \sqrt{\frac{\displaystyle\sum_{i=1}^{\check{n}} w_i \left(x_i - \bar{x}_w\right)^2}{\dfrac{(\check{n}-1)}{\check{n}} \displaystyle\sum_{i=1}^{\check{n}} w_i}}, \tag{6.17}$$
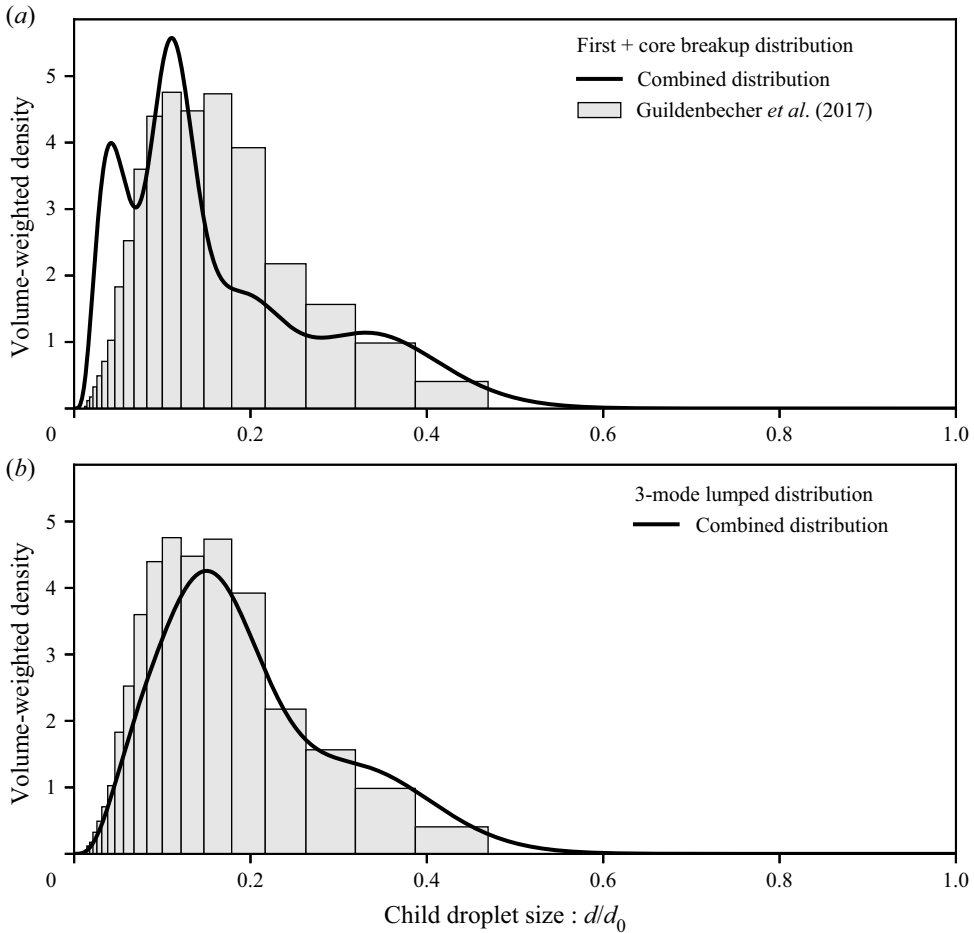
Figure 26. Comparison of the present predictions for (*a*) the combined distribution and (*b*) the combined lumped distribution with measurements from Guildenbecher *et al.* (2017) for ethanol drops of initial diameter $d_0 = 2.55$ mm at $We = 55.3$.

respectively, where the characteristic sizes of each mechanism are calculated as before, and the weights are calculated by dividing the mode weight by the number of mechanisms that contribute to that mode (i.e. each mechanism within a mode is weighted equally, as before). The combined lumped distributions are compared with the data of Guildenbecher *et al.* (2017) in figure 26(*b*). As expected, the distribution that results from lumping overlapping modes together gives a better prediction of the distribution for $d/d_0 < 0.2$, as the effect of the misprediction of the contributions of the bag and rim modes is reduced.

6.4. *Summary of distribution prediction*

In the present work, the distribution of sizes resulting from droplet breakup is assumed to come from a combination of a plethora of mechanisms as well as subtle variations within each mechanism. These mechanisms are grouped in terms of the primary modes of the breakup (i.e. the geometries within the deformed droplet) such that the overall distribution is the result of the sum of the modes, which can lead to a multimodal distribution. While the volume weighting of each mode is determined by models for the volume estimation

of each geometry, the relative number weighting of the mechanisms within each mode is assumed to vary as a two-parameter gamma distribution function where the parameters are estimated based on the mean and standard deviation of the predicted sizes for each mechanism within the mode. In bag breakup, there are three modes resulting from the rim nodes, the remaining rim and the bag. In MB breakup, there is the addition of the breakup of the undeformed core, which itself breaks into an additional three modes. However, in MB breakup, several of the modes overlap. When two or more modes overlap such that they appear as one, the weighted mean and standard deviation of the mechanisms contributing to each mode can be used to determine a lumped distribution that captures the overlapping modes as one. Figure 27 gives a flowchart of the calculation of the multimodal distribution.

7. Conclusions

Although there have been many previous works that have sought to theoretically model the aerodynamic breakup of droplets, none have been able to predict the distribution that results from the breakup. Among the limiting factors of previous works is the focus on one specific mechanism of the breakup; typically, the breakup of the rim by the Rayleigh–Plateau capillary instability. As a result, previous theoretical works have formulated predictions of only single characteristic sizes of the breakup. Following our previous work (Jackiw & Ashgriz 2021), which developed models for predicting the primary geometries that form in the aerodynamic breakup of drops (i.e. the rim and bag), the present work has investigated a variety mechanisms that lead to the breakup of these geometries. Three key geometries were investigated: the rim nodes, the bag and the remaining rim.

Zhao *et al.* (2010) have previously studied the formation of nodes on the rim, where the instability was assumed to be of a Rayleigh–Taylor type due to the rim's acceleration. In the present work, the Rayleigh–Plateau instability was shown to also give a reasonable prediction for the number of nodes formed on the rim. However, since a portion of the rim remains between the nodes when they separate, the classical Rayleigh–Plateau mechanism does not give a good prediction of the node droplet sizes. In the present work, only a portion of the rim segment within each instability wavelength was assumed to form the node droplet. The volume fraction of the segment that forms a node was determined empirically by relating the volume of the node child droplets to the volume of the windward disk. As a result, the size of the node child drops was predicted. It was shown that the variation in the node sizes is related to the variation in the node volume fraction.

The breakup of the bag in aerodynamic droplet breakup has not been studied extensively due to limitations in imaging capabilities; although, many other works have studied the similar geometry of the breakup of a surface bubble. In the present work, the model of Wang *et al.* (2018) for the formation of the receding rim at the front of the bag perforation and its instability was compared with measurements of the bag recession and instability wavelength, with a favourable agreement indicating that the dynamics are indeed similar. Using this analysis, the minimum thickness of the bag was estimated as $\bar{h}_{min} = 2.3 \pm 1.2$ μm. It is proposed that the variation in sizes that results from the breakup of the bag is due to variations in the bag thickness and the production of child droplets of the order of the receding rim thickness and the bag thickness, as well as the formation of child droplets in the breakup of the receding rim.

Previous models for the breakup of the rim have focused only on the Rayleigh–Plateau instability mechanism (Chou *et al.* 1997; Jackiw & Ashgriz 2021; Obenauf & Sojka 2021);
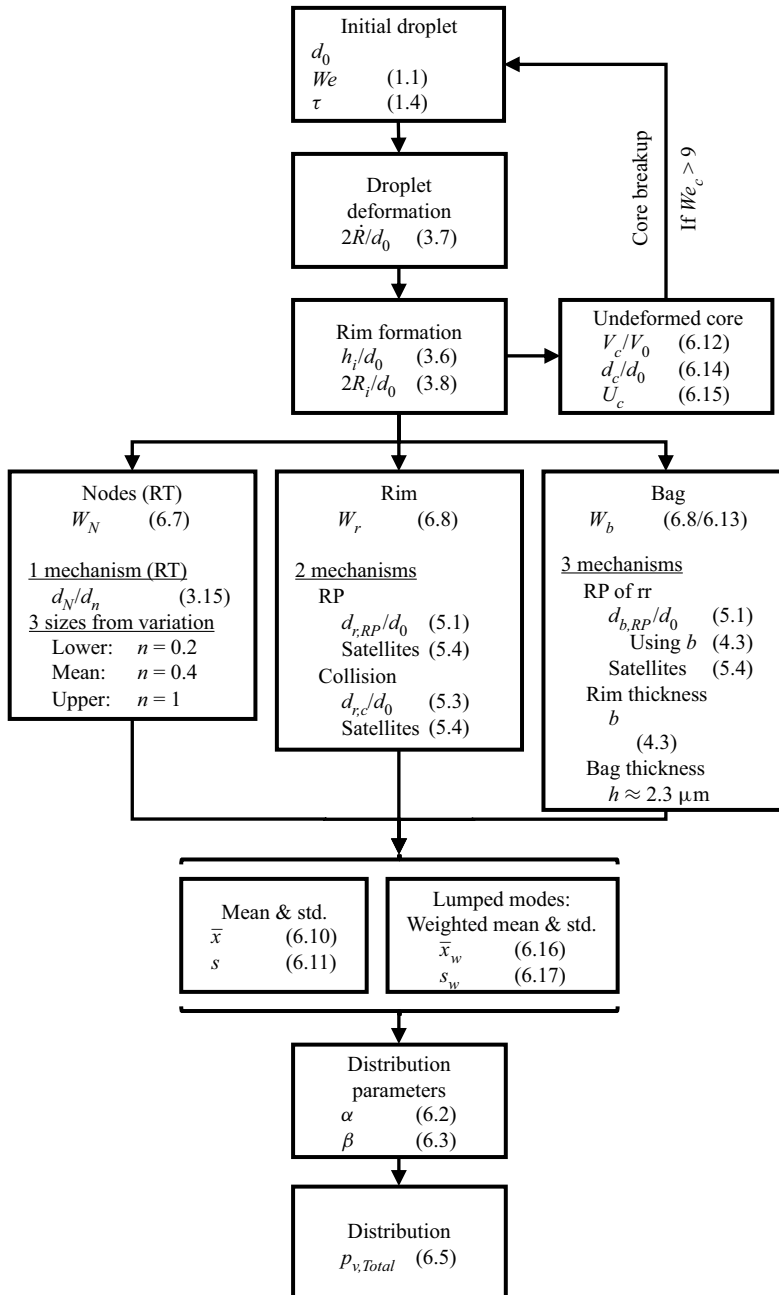
Figure 27. Flowchart for the calculation of the multimodal size distributions.

however, this mechanism has been found to somewhat over-predict the mean size of the rim's child droplets. In the present work, an additional mechanism is considered, wherein the receding rim, corrugated due to its own instability, collides with the rim and imparts a strong disturbance at the same wavelength as the receding rim's instability, which ultimately dominates the rim's breakup. The breakup of the rim was thus shown to be the result of a combination of the described collision mechanism and the Rayleigh–Plateau

mechanism, when the rim recedes along the rim without a significant collision, as well as the formation of satellite droplets under each mechanism.

Using the combination of the above mechanisms for each of the modes of the breakup, the distribution of the breakup was predicted semi-analytically. Each mode was modelled as a monomodal distribution using the algebraic mean and standard deviation of the constituent mechanisms to approximate the relative weighting of the mechanisms as a two-parameter gamma distribution. The relative contribution of each mode was estimated by the volume fraction of the parent droplet that each mode represents. The weighted sum of the three primary modes then gives a multimodal distribution, which was found to agree favourably with the experimental distribution measurements of Guildenbecher *et al.* (2017). At higher-*We* conditions, such as in MB breakup, an undeformed core can remain after the initial breakup of the periphery. The aerodynamic conditions of the core were estimated based on the predicted volume of the core and the speed of the droplet at the end of the first breakup phase as a result of drag. Under these conditions, the distribution then has six modes: three for the initial breakup and three for the core. Since the sizes of some of the modes, in particular the bag and rim sizes, are close, their combined distributions appear as a single mode. In these cases, the overlapping nodes can be lumped together as a single mode, where its parameters were estimated by a weighted mean and standard deviation. The model including the core breakup for MB breakup was also found to agree favourably with the experimental distribution measurements of Guildenbecher *et al.* (2017)

A summary of the mechanisms involved in aerodynamic droplet breakup as they are studied in the present work is given graphically by the flowchart in figure 28.

7.1. *Opportunities for future work*

Although the present work was developed in an effort to be primarily analytical, some empiricisms had to be made along the way in order to account for dynamics that are not yet well understood. As a result, the effects of conditions not studied in the present work such as high *Oh* or ambient density on the individual mechanisms and on the model as a whole are not known. However, every effort was made to ensure that the empiricisms be related directly to physical phenomena, rather than simple corrections to improve the fit of the models. In doing so, opportunities for further research become apparent. Further development of the understanding and modelling of these areas will offer meaningful insight and the potential for widely applicable models for atomization.

While not explicitly part of the present work, the authors' prior model for the deformation of the droplet (Jackiw & Ashgriz 2021) employs some empiricisms to account for such unknown dynamics. Firstly, the 'flow-balancing time' (the prefactor in (3.7)) is an estimate of the transient deformation that precedes the constant-radial deformation rate; however, the dynamics that leads to its value is not modelled. Next, the extent of deformation at initiation is also partially empirical, since the dynamics that leads to the precise combination of $2R_i$ and h_i is unknown; although, it is known that they are coupled, which allows for the determination of h_i from the empirical correlation for $2R_i$ (equation (3.8)). However, this determination also requires some empiricism to account for the effect of the wake separation, which leads to the -0.05 term in (3.6) as discussed in Appendix A. Although viscosity is not expected to play a significant role in these factors, a higher density in the surroundings such as in extremely high-pressure conditions is likely to.

The flow dynamics of and interaction between the rim, nodes and bag geometries are another area where empiricism was used in the present work to account for the unknown dynamics. The parameters *n* and *m* were used to express the flows between the rim and
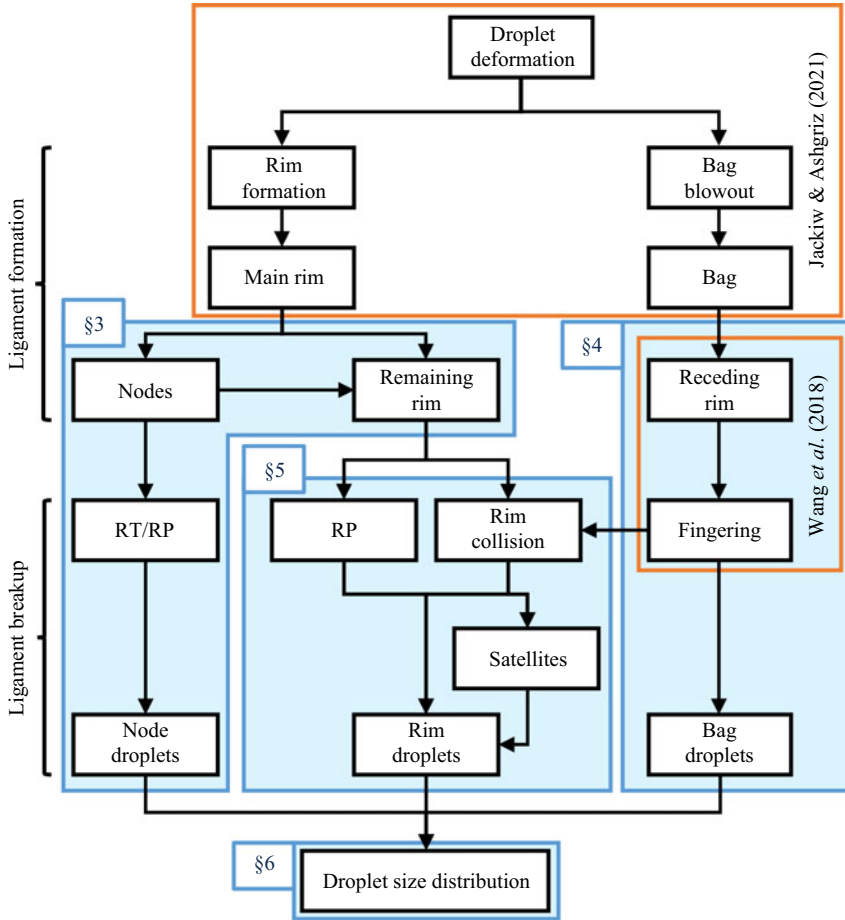
Figure 28. Flowchart showing the processes involved in aerodynamic droplet breakup. Blue boxes denote the relevant sections of the present work. Orange boxes indicate the previous studies used in the present study.

the nodes, and by extension the bag, where $n = m = 0.4$ was determined empirically and appears to be relatively constant for the present range of We; however, these dynamics may vary in cases where the breakup times are longer such as at high Oh. Additionally, the effect of folds in the bag as a result of an undeformed core on these flow dynamics has not been studied, and was neglected in the present work.

Furthermore, the dynamics leading to the rupture of the bag is not well known. In the present model, the coefficient C in (4.7) is used to fit the piercing time of a Rayleigh–Taylor instability on the expanding bag to the bag lifetime (see Jackiw & Ashgriz 2021; Vledouts *et al.* 2016), while the minimum bag thickness was empirically taken to be constant as $h_{min} = 2.3 \pm 1.2\ \mu m$. Although the mechanisms leading to the rupture of films in surface bubbles have been studied widely, the dynamics of a quickly inflating bag in an air stream is significantly different and remains to be revealed.

Finally, the selection of the gamma distribution function when modelling the breakup size distribution is, in a way, an empiricism in that it is an assumption of how the mechanisms used to determine its parameters are distributed relative to each other. Although the gamma distribution is one of the primary distributions used in the literature to fit droplet size distributions, it is important to note that several other distributions are

commonly used as well (for instance, log-normal and root-normal), and that truncated or bounded distributions may provide a more physical representation of the phenomenon, although they are yet to be applied widely. By extension, the process of lumping modes together, which offers a better prediction especially at high *We* where there is significant overlap in the modes, as carried out in § 6.3, is also an empirical process. Further work on objectively and programmatically identifying when modes can be lumped together, as well as selecting appropriate distribution functions, will greatly benefit future generations of the present model.

Declaration of interests. The authors report no conflict of interest.

Author ORCIDs.
ⓘ Isaac M. Jackiw https://orcid.org/0000-0002-8552-1723;
ⓘ Nasser Ashgriz https://orcid.org/0000-0002-5661-4453.

Appendix A. Modifications to model of Jackiw & Ashgriz (2021)

In the model of Jackiw & Ashgriz (2021), based on the average of the experiments across the bag and BS morphologies, the extent of the cross-stream deformation at initiation was found approximately as $2R_i/d_0 \approx 1.6$. Although this gives acceptable results throughout the rest of the analysis, it assumes that $2R_i/d_0$ is constant for all *We*. Although this is a reasonable approximation for $We > 12$, the experimental values for $2R_i/d_0$ are slightly less at lower *We*. As a result, a modification is made wherein $2R_i/d_0$ is fitted by the asymptotic function

$$\frac{2R_i}{d_0} = c_1 - (c_1 - c_2)\exp(-c_3 We), \tag{A1}$$

where c_1 is the maximum value of $2R_i/d_0$, c_2 is the theoretical value of $2R_i/d_0$ at $We = 0$ and c_3 is the rate at which $2R_i/d_0$ reaches c_1. Note that the theoretical value of $2R_i/d_0$ at $We = 0$ is non-physical, as the regime of the deformation must transition to oscillatory at low *We*, where the definition of initiation no longer exists. The fit of (A1) to the data of Jackiw & Ashgriz (2021) for bag and BS data gives $c_1 = 1.63$, $c_2 = -1.25$ and $c_3 = 0.312$. The resulting fit is compared with the constant value of $2R_i/d_0 = 1.6$ given by Jackiw & Ashgriz (2021) and with the model for the maximum extent of cross-stream deformation ((3.4); Zhao *et al.* 2010) in figure 29(*a*).

Additionally, in the analysis of Jackiw & Ashgriz (2021), the prediction of h_i/d_0 was found to be slightly high due to the effects of the wake being neglected in the pressure balance. An empirical correction of -0.05 in (3.6) is applied to the model to account for these effects. The uncorrected model of Jackiw & Ashgriz (2021) along with its first correction ($h_i/d_0 - 0.05$) and the presently used modified model incorporating this correction and the asymptotic fit of $2R_i/d_0$ (equation (A1)) are compared with the data of Jackiw & Ashgriz (2021) for bag and BS breakup in figure 29(*b*). Although the present model and theory focus on the breakup mechanisms at lower *We*, where they have been resolved, it is important to note that this wake-pressure correction will result in non-physical values at high *We* ($We > 200$), as (3.6) will become < 0. This is likely because the wake pressure at high *We* instead leads to the shearing of the periphery
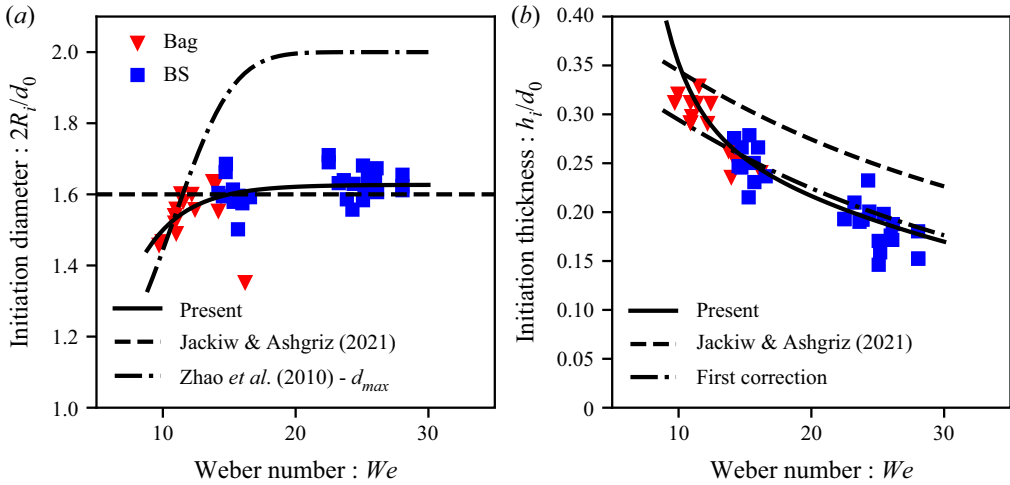
Figure 29. (*a*) Initiation diameter versus *We*, compared with correlations of Jackiw & Ashgriz (2021) (equation (3.8)) and Zhao *et al.* (2010) (equation (3.4)). (*b*) Initiation thickness versus *We* compared with semi-empirical equation of Jackiw & Ashgriz (2021) (equation (3.6)).

downstream from the droplet, and thus the assumed pressure correction does not hold. Further investigation into the initiated rim thickness, as well as the many other mechanisms described in the present work, is required to develop the model for high *We*.

Marcotte & Zaleski (2019) also provided an analysis of the rim dynamics, which was not previously compared in Jackiw & Ashgriz (2021), that used a similar pressure balance across the rim to estimate the transition to the ST morphology. In their analysis, it is proposed that the Dimotakis velocity, $\dot{R} = U\sqrt{\rho_g/\rho_l}$ for $\rho_g \ll \rho_l$, could be used to predict the constant radial expansion rate of droplets undergoing aerodynamic breakup. However, as shown in figure 30(*a*), the Dimotakis velocity over-predicts $\dot{R}$; therefore, the model of Jackiw & Ashgriz (2021) (equation (3.7)) will be used instead. Their analysis supposes that the transition to the ST morphology occurs when the rim forms at the periphery, which is supposed to occur when the curvature pressure balances with the radial inertia, $\rho_l \dot{R}^2 \propto \sigma h_i/2$ (which can be recast as $h_i/d_0 = 2/We_{rim}$ to be compared to (3.6)). In their analysis, the azimuthal curvature is neglected since their model is compared with a two-dimensional numerical simulation where the azimuthal direction is not included. For the high *We* at which the ST transition occurs, this assumption is satisfactory, as the thickness curvature is dominant over the thickness curvature at this range. Additionally, the air pressure at the periphery and the wake is neglected. Using the prediction of $\dot{R}$ by Jackiw & Ashgriz (2021) (equation (3.7)) in their expression for h_i provides satisfactory agreement for the intended range at $We \approx 80$, but over-predicts the data at low *We*. This is expected due to the omission of the air pressure at the periphery and of the azimuthal curvature. However, as $We \rightarrow \infty$, the model of Marcotte & Zaleski (2019) asymptotes to $h_i \rightarrow 0$, and thus may give satisfactory agreement for the high-*We* range where the present model fails due to the constant wake-pressure correction mentioned previously. This may suggest that the periphery air pressure, omitted by Marcotte & Zaleski (2019), is effectively cancelled by the wake pressure at high *We*. Although such high-*We* dynamics is outside of the present scope, the model of Marcotte & Zaleski (2019) for the initiation thickness, using the model of Jackiw & Ashgriz (2021) for the radial expansion rate, may be more appropriate at higher *We*.
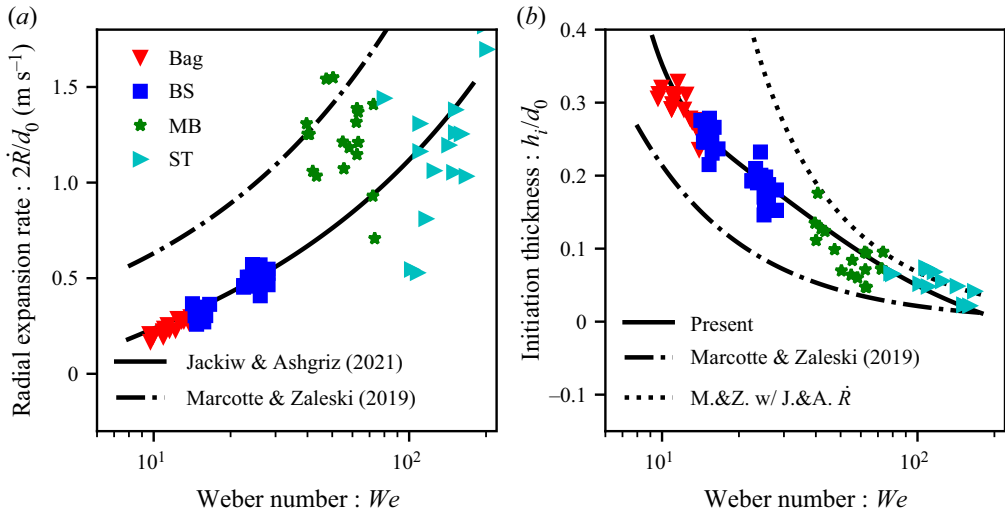
940 A17-48

Figure 30. Comparison of (*a*) radial deformation rate and (*b*) initiation rim thickness models of Jackiw & Ashgriz (2021) and Marcotte & Zaleski (2019).
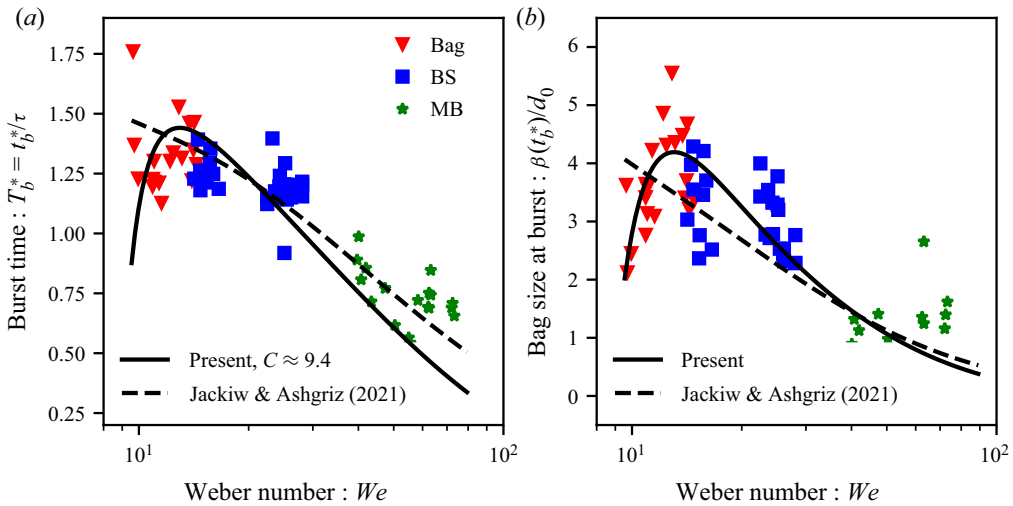

Figure 31. Comparison of modified and unmodified models of Jackiw & Ashgriz (2021) for (*a*) T_b^* (equation (4.7)) and (*b*) $\beta(t_b^*)/d_0$ (equation (4.5)).

Since the models for $2R_i/d_0$ and h_i/d_0 have been modified, the effects of the modifications on the later empirical fit of the bag blow-out time (C in (4.7)) must also be considered. Propagating the modified $2R_i/d_0$ and h_i/d_0 through the model of Jackiw & Ashgriz (2021) results in a new value for $C \approx 9.4$. The resulting modified breakup time and bag size at burst (equation (4.5)) predictions are compared with the unmodified model of Jackiw & Ashgriz (2021) in figure 31.

The prediction at low *We* for both the burst time and the bag size at burst is improved, where the modified model more accurately predicts the downturn of the trend at low *We*. Notably, the prediction for both approaches 0 near $We_c \approx 8.8$. This is significant since it
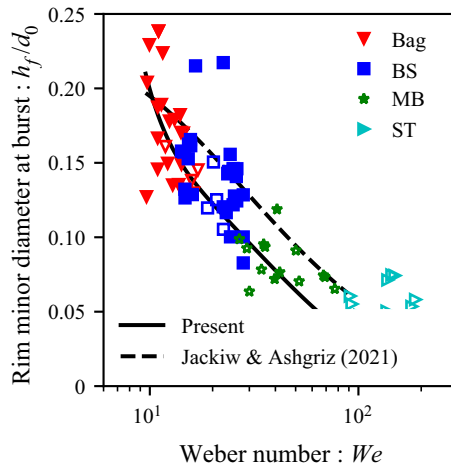
Figure 32. Comparison of modified and unmodified models of Jackiw & Ashgriz (2021) for h_f/d_0 (equation (3.18)).

matches the expected trend of the physical limit where the bag does not form for $We < 8.8$, suggesting that the earlier modifications lead to a more physically accurate model overall.

Finally, the modified model for the rim minor diameter at burst, h_f/d_0 (equation (3.18)), is compared with the unmodified model of Jackiw & Ashgriz (2021) in figure 32. This is included as it is important to the analysis of § 5.

Appendix B. Comparison of instability theories for node formation

In previous investigations of the rim nodes, the instability has been assumed to be of a Rayleigh–Taylor type (Zhao *et al.* 2010) due to the acceleration of the deforming droplet in the air stream; however, it is also possible that a Rayleigh–Plateau type of instability causes the rim's corrugation. There is also the question of at what time the instability takes hold, as its dimensions, and thus maximum susceptible wavelength for both the Rayleigh–Taylor and Rayleigh–Plateau instabilities, change as the rim expands throughout its lifetime. While § 3 gives a detailed comparison of the Rayleigh–Taylor and Rayleigh–Plateau instability theories using their most suited extent of deformation, this appendix gives a more in-depth review of how the selection of the extent of deformation affects the instability predictions.

The problem of identifying the extent of the droplet deformation presents a difficulty stemming from an inconsistency in the literature in defining the moment in the deformation that the rim becomes susceptible to instability. The geometry of the droplet at this instant in the cross-stream ($2R$) and streamwise (h) directions is henceforth referred to as the critical geometry. Note that, in many works, this instant is also referred to as the initiation time; however, since the present work considers the critical moment at which the instability takes hold on the rim rather than the moment at which the breakup phase initiates (a subtle difference that will become clear throughout this appendix), we chose to define these instances uniquely.

In previous works applying the instability wavelength to a deforming droplet (Theofanous *et al.* 2004), and in particular the work of Zhao *et al.* (2010) who applied the analysis to the rim as in the present analysis, it is argued that the instability takes hold at the maximum cross-sectional dimension of the droplet achieved prior to breakup,

$2R_{max}$. This extent of deformation theoretically corresponds to the maximum acceleration of the deforming droplet prior to the blow-out of the bags, and thus makes sense with respect to the driving mechanism behind the Rayleigh–Taylor instability. In older works, this geometry defines the initiation time.

The most commonly used empirical correlation for $2R_{max}$ was determined by Hsiang & Faeth (1992) for $We < 100$ as

$$\frac{2R_{max}}{d_0} = 1 + 0.19\sqrt{We}. \tag{B1}$$

However, Zhao *et al.* (2010) found that (B1) only applied to their results for $We < 20$, where for $We > 20$, $d_{max}/d_0 \approx 2$, which agrees with the results of Dai & Faeth (2001) of $d_{max}/d_0 = 2.15$ for $20 < We < 80$. As a result, Zhao *et al.* (2010) provided an alternative empirical correlation, given in § 3 by (3.4). Although Zhao *et al.* (2010) formulated the correlation of (3.4), the correlation of Hsiang & Faeth (1992) (equation (B1)) was used in their analysis for predicting N. In the present work, it is found that the correlation of Zhao *et al.* (2010) (equation (3.4)) is better suited for the model to predict N, as it more accurately captures the droplet deformation at $We < 15$. Therefore, the model using the correlation of Hsiang & Faeth (1992) (equation (B1)) is omitted from the analysis in this appendix, although it is compared with the models presented in the present work in § 3.

More recent analyses of droplet breakup have proposed an alternative definition of the critical geometry in droplet breakup, where the initiation time is defined instead by the minimum streamwise thickness of the droplet (Flock *et al.* 2012; Jackiw & Ashgriz 2021). This is taken to be the true instant of initiation, assigned the subscript i, as it has been shown to be useful in predicting the breakup morphology (Jackiw & Ashgriz 2021). In this view, the critical cross-stream dimension, d_i, is somewhat smaller than the maximum dimension proposed in earlier works. For a more detailed discussion of the differences in these definitions, see Jackiw & Ashgriz (2021). The critical cross-stream dimension given by this dimension is then the same as defined in the modified model of Jackiw & Ashgriz (2021) as given by (3.8) (see Appendix A)

The existing correlations for the streamwise thickness of the droplet, h, for the maximum critical deformation relate h to $2R$ through conservation of mass with the initial droplet volume assuming an ellipsoid cross-section. However, Jackiw & Ashgriz (2021) showed that, for the maximal deformation, volume is not conserved between these shapes owing to an undeformed core at the centre of the deforming droplet. As a result, only the minimum streamwise thickness, h_i, is appropriate for estimating the thickness of the rim. The modified semi-empirical relationship by Jackiw & Ashgriz (2021) for the rim thickness is provided by (3.6).

Considering the two instability mechanisms being investigated (Rayleigh–Taylor and Rayleigh–Plateau) and the two definitions of the extent of deformation ($2R_{max}$ and $2R_i$) at which the instability takes hold, four possible cases are derived and are tabulated in table 6. The Rayleigh–Taylor (equation (3.13)) and the Rayleigh–Plateau (equation (3.14)) instability models predicting N are compared for the four cases tabulated in table 6 with the experimental measurements of the present analysis as well as the measurements of Dai & Faeth (2001) and Zhao *et al.* (2010) in figure 33. Note that while the models are shown as continuous in N, they represent discrete steps in N, as N must be a whole number.

The results of figure 33 provide a basis for comparing the cases of table 6. Considering the differences in the definition of the critical geometries ($2R_{max}$ and $2R_i$) for the Rayleigh–Taylor instability (cases 1 and 2, respectively), the maximum deformation (case 1) is seen to better predict N, using (3.13), than the initiation deformation (case 2). This is sensible for the definition of the Rayleigh–Taylor instability, as the maximum drag
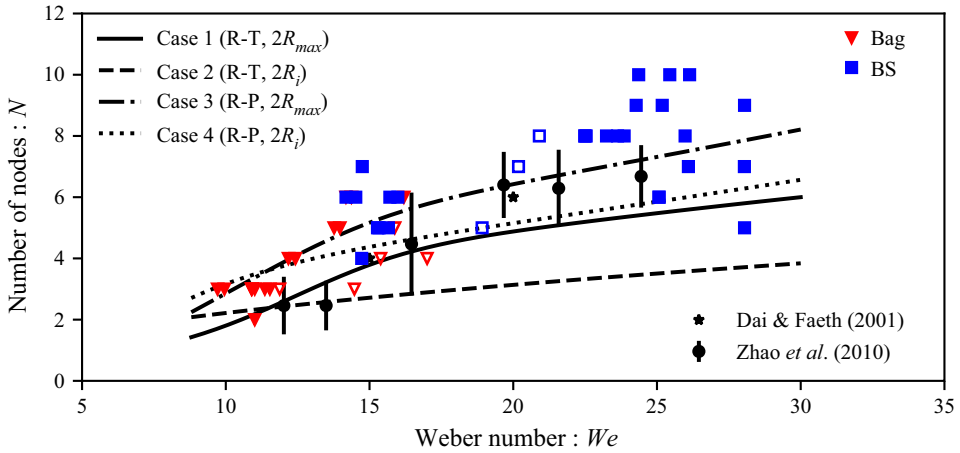
Figure 33. Number of nodes, N, versus We for the four cases tabulated in table 6 for the Rayleigh–Taylor (equation (3.13)) and the Rayleigh–Plateau (equation (3.14)) instabilities.

Case	Instability		d	
1	Rayleigh–Taylor	(equation (3.3))	$2R_{max}$	(equation (3.4))
2	Rayleigh–Taylor	(equation (3.3))	$2R_i$	(equation (3.8))
3	Rayleigh–Plateau	(equation (3.5))	$2R_{max}$	(equation (3.4))
4	Rayleigh–Plateau	(equation (3.5))	$2R_i$	(equation (3.8))

Table 6. Model cases for node instability.

coefficient and frontal surface area, and thus the maximum acceleration, are achieved at $2R_{max}$. In other words, the strength of the Rayleigh–Taylor instability is at its greatest at $2R_{max}$, at which point the instability takes hold and develops the nodes on the rim. In this way, even if the rim were unstable due to Rayleigh–Taylor instability at the initiation deformation, it will be more unstable at the maximum deformation, and thus the instability at the maximum deformation will dominate.

The differences in the definition of the critical geometries ($2R_{max}$ and $2R_i$) for the Rayleigh–Plateau instability (cases 3 and 4, respectively), however, are less clear. While the prediction of N assuming the maximum deformation (case 3), using (3.14), generally provides a better prediction of the mean of the spread of the results than the other cases, the prediction assuming the initiation deformation (case 4) is still within the spread of the results, near their lower limit. In fact, case 4 is nearly identical to case 1 for $We > 15$. Furthermore, both geometries are plausible with regards to the physics of the Rayleigh–Plateau instability. In the case of the rim dynamics being governed by the initiation geometry, the instability would be presumed to take hold at the instant the rim forms. For the maximum deformation scenario, the instability would take hold shortly after the rim has formed, when the initially thick windward disk will have thinned, isolating the toroidal shape of the rim from the sheet, which may be able to damp the instability and suppress the formation of the nodes at the initiation geometry (see Appendix B.1). Since the results are so similar between cases 3 and 4, and since there is no evidence refuting the plausibility of either scenario, it cannot be concretely determined from the present data and

analysis as to which scenario is more likely to govern the theory of the Rayleigh–Plateau instability of the rim.

Comparing the differences between the Rayleigh–Taylor (case 1) and Rayleigh–Plateau (cases 3 and 4) instability theories, there is again not enough of a difference between the predictions to conclude which is dominant. As mentioned earlier, the Rayleigh–Taylor theory using the maximum deformation (case 1) provides a nearly identical result to the Rayleigh–Plateau theory using the initiation deformation (case 3), with the exception of the range $We < 15$ where the two theories deviate. The Rayleigh–Plateau theory using the maximum deformation (case 3) gives a better prediction of the mean spread of the data for $We > 15$ than the other cases, but over-predicts for $We < 15$. This over-prediction could be the result of the enhanced stability of low-aspect-ratio tori, such as those formed by the rim at low We. This effect is discussed further, qualitatively, in Appendix B.1. Such instabilities of low-aspect-ratio tori are not yet well understood and their investigation has so far been limited to experimental and numerical works, which have not resulted in analytical predictions of the modified instability wavelength. Therefore, this stabilizing effect on the rim cannot be quantified given the present analysis. The proposition as to which instability mechanism is dominant is thus limited to a degree speculation, and both theories can provide comparable results in terms of predicting the number of nodes formed.

Although the models presented here generally under-predict the data for N, several stabilizing effects have been neglected; however, as is discussed in Appendix B.1, these effects can only be compared with the present cases qualitatively.

B.1. *Rim stabilizing effects*

The present work neglects a few potential stabilizing effects to the applied instability theories. This appendix provides an overview of some of the stabilizing effects that may exist in aerodynamic droplet breakup. In the case of the mechanisms discussed here, either the present data are insufficient to determine their effect, or the existing analyses are insufficient to quantify the effect for the present case.

From previous works on the Rayleigh–Plateau instability in liquid columns, the stretching of the column can tend to stabilize the column against the capillary instability if the stretching rate is faster than the rate of capillary thinning of the column (Villermaux, Pistre & Lhuissier 2013; Keshavarz *et al.* 2020). In the present scenario, the rim stretches as it expands, which may tend to stabilize the rim. The stretching rate of the rim, $\dot{\epsilon}$, can be estimated from the its expansion rate, given by (3.7) (Jackiw & Ashgriz 2021) as $\dot{\epsilon} = \pi\dot{d}$, while the capillary thinning rate is given by Keshavarz *et al.* (2020) as $1/\sqrt{8\rho_l h^3/\sigma}$. However, for the present cases, the stretching rate is much less than the capillary thinning rate; therefore, the stability of the liquid rim is unaffected by its stretching.

In the present analysis, the rim was assumed to be slender enough that it could be approximated by a cylindrical column; however, for sufficiently low We, the AR of the rim may be low enough such that the assumption does not hold. Such tori are more stable against the Rayleigh–Plateau instability owing to the additional curvatures compared with a slender torus, which is more similar to a liquid column with periodic symmetry (Mehrabian & Feng 2013). In the low-AR limit, the torus will collapse into a single droplet. This limit may be a factor in the minimum geometry required for the formation and breakup of the rim. The instabilities of low-aspect-ratio tori are not yet well understood, and their investigation has so far been limited to experimental and numerical works, which have not resulted in analytical predictions of the modified instability wavelength.

As was determined in § 3, there is mass transfer into the rim from the bag, accompanied by mass transfer from the rim into the nodes. Savtchenko & Ashgriz (2005) showed that liquid columns can be stabilized by the transfer of mass into the column (e.g. from the bag to the rim), or destabilized by the transfer of mass out of the column (e.g. from the rim to the nodes). Since the temporal properties of the bag are unknown in the present case (e.g. the bag thickness and mass flow rate into the rim), their analysis cannot be compared quantitatively with the present results. However, it is worth noting that this stabilizing effect may arise in the case of both the instability of the main rim as well as the instability of the receding rim of the bag, which is discussed in § 4.

The bag also has a potentially stabilizing effect on the rim due to the geometry of the rim being modified where it meets the bag (see figure 17). This was discussed in detail in § 5 with respect to the main rim; however, this effect will also arise in the instability of the receding rim.

Appendix C. Comparison of theories for the instability of the receding rim

The case of the instability of the receding rim has been studied for other contexts, such as for the edge of planar sheets (Lhuissier & Villermaux 2009, 2011; Wang *et al.* 2018) and for surface bubbles (Lhuissier & Villermaux 2012); however, these studies have not been compared with the present case of the breakup of bags in aerodynamic droplet breakup. Most of these studies have considered the rim to be unstable to the Rayleigh–Taylor instability. The wavelength of the Rayleigh–Taylor instability is given by (3.3) and depends on the acceleration, a. The variations in the previous studies of this phenomenon centre around proposing different causes for the acceleration that leads to the instability. In this appendix, these theories are compared with the breakup of bags in aerodynamic droplet breakup.

Lhuissier & Villermaux (2009) showed that, for a liquid sheet containing surfactants, the apparent rim at the receding edge of a liquid sheet is actually a wave that has formed at and parallel to the edge. They proposed that this waving was the result of a Kelvin–Helmholtz shear instability as a result of the induced shear between receding edge and surroundings, and that the flapping motion results in the acceleration of the edge of the sheet, which in turn causes the Rayleigh–Taylor instability. Using the appropriate scaling laws for each instability mechanism, Lhuissier & Villermaux (2009) found the wavelength of receding 'rim' to be

$$\lambda_{rr} = \frac{1}{2} \frac{\sigma}{\rho_g u_{rr}}, \tag{C1}$$

where the coefficient $1/2$ is applied to the general scaling law to match their data. This coefficient is included implicitly in their plots but is not mentioned explicitly in their work. Lhuissier & Villermaux (2009) note that the flapping instability should only occur when the Weber number of the receding edge is $We = \rho h u^2 / \sigma > 2$; however, using the Taylor–Culick law (equation (4.1)) always results in $We = 2$. It may be the case that this flapping phenomenon only occurs for surfactant-laden sheets; however, no further studies have been carried out to show whether or not this is the case. We note that the liquid sheet thicknesses studied by Lhuissier & Villermaux (2009) are of the same order as those in the present work (1–10 μm). Although Lhuissier & Villermaux (2009) provide an interesting view of the dynamics of liquid sheet retraction, subsequent works have not considered, or revealed, this flapping phenomenon.

Later, the same researchers (Lhuissier & Villermaux 2011) proposed an alternative view that the accelerating force comes instead from the acceleration of the initially
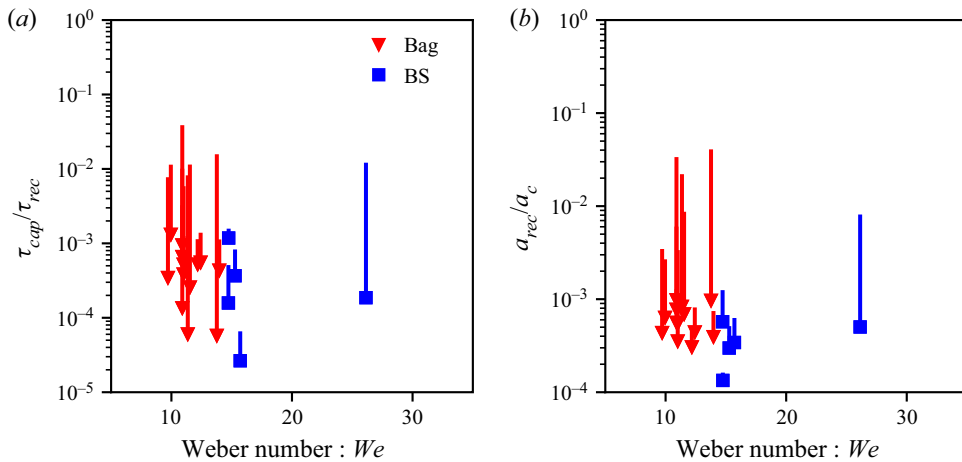
Figure 34. (*a*) Comparison of capillary time with bag recession time. (*b*) Comparison of bag recession acceleration with centripetal acceleration. The vertical bars show the time variation in each, where the marker indicates the initial value.

stationary sheet edge to the Taylor–Culick recession speed, u_{rr} (from (4.1)). The resulting Taylor–Culick acceleration is given by

$$a_{TC} = \frac{8\sigma}{\pi \rho_l h^2}. \tag{C2}$$

A feature of this acceleration is that the approximate time required to achieve the steady recession speed is the capillary time, $\tau_{cap} = \sqrt{\rho_l h^3 / \sigma}$. The capillary time for the present experiments is much smaller than the recession time of the bag ($t_{cap}/t_{rec} < 0.01$) as shown in figure 34(*a*). Indeed, the capillary time is also less than the elapsed time between the images ($\tau_{cap}/t_{FPS} < 0.1$); thus the initial acceleration is not resolvable in the present experiments. Since the capillary time is so small relative to the other time scales of the experiment, it is reasonable to assume that the changes in the velocity of the receding rim due to changes in the bag thickness will occur essentially instantaneously, i.e. the recession velocity at each bag thickness is in a quasi-steady state, allowing (4.1) to hold even though the thickness is varying as the rim recedes.

Additionally, Lhuissier & Villermaux (2011) showed that a similar result can be achieved by assuming that the receding rim is susceptible to the Rayleigh–Plateau instability, rather than to the Rayleigh–Taylor instability. Basing the Rayleigh–Plateau wavelength (equation (3.5)) on the initial rim thickness (i.e. the bag thickness), a nearly identical scaling law is found ($\lambda_{RT} \approx 6.82h$ versus $\lambda_{RP} \approx 4.5h$), suggesting that the two mechanisms are 'intrinsically undistinguishable' (Lhuissier & Villermaux 2011). This result is especially notable when compared to the present result of § 3, where the two instabilities were also shown to be essentially identical when used to analyse the instability of liquid tori.

While both of the above theories were developed primarily for the recession of planar sheets, alternative theories have also been proposed for recessions around spherical caps, i.e. for surface bubbles. Again, the same researchers (Lhuissier & Villermaux 2012) suggested that, in the case of recession around a spherical cap, the acceleration is due to the centripetal acceleration that the rim experiences as it follows the hemispherical shape, given by (4.2). Lhuissier & Villermaux (2012) then scale the wavelength, based
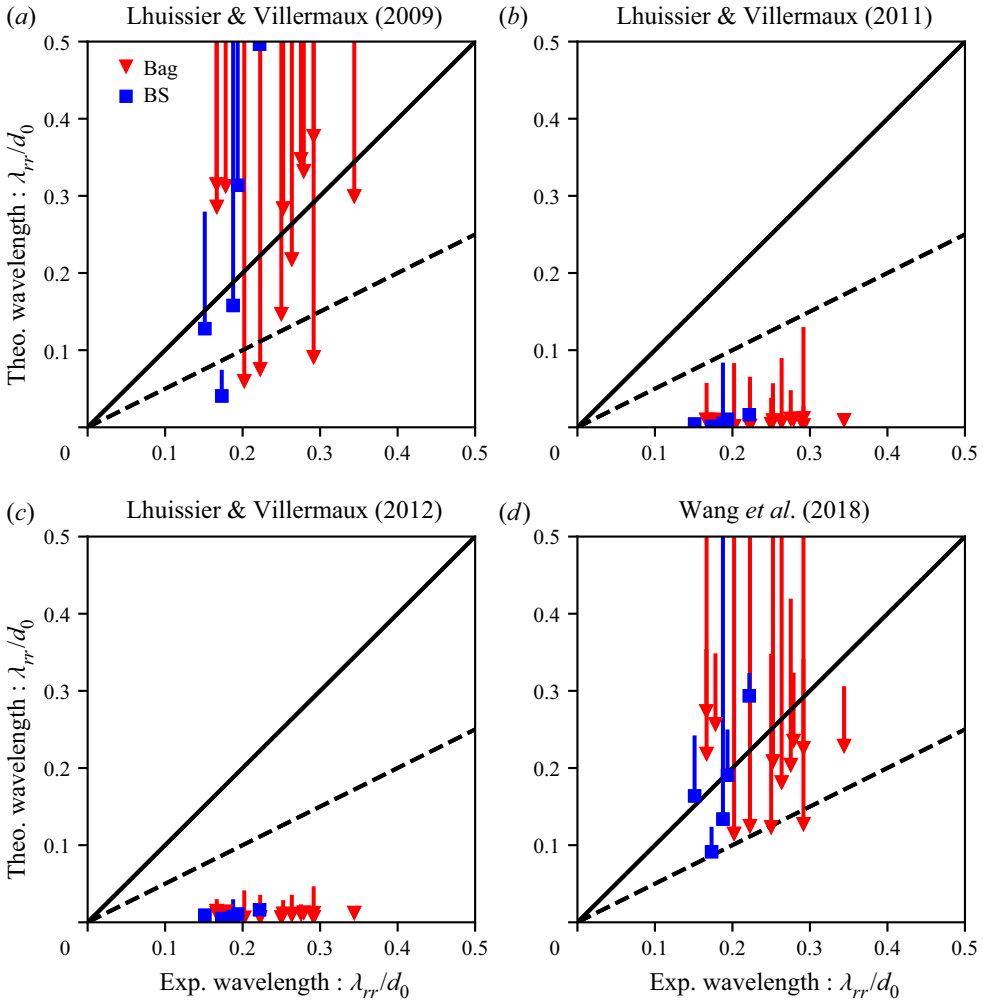
940 A17-55

Figure 35. Comparison of models for λ_{rr}. The solid line shows unity in comparison while the dashed line represents the upper measurement limit of 2λ. (*a*) Lhuissier & Villermaux (2009) (equation (C1)), (*b*) Lhuissier & Villermaux (2011) ((3.3) using (C2)), (*c*) Lhuissier & Villermaux (2012) (equation (C3)) and (*d*) Wang *et al.* (2018) ((4.4) using (4.3) and (4.2)). Markers indicate the initial value, which gives the highest acceleration (h_{min} or $u_{rr,max}$), and the vertical bars indicate the time variation to the minimal acceleration (h_{max} or $u_{rr,min}$). Calculations are based on experimental measurements of u_{rr} and R.

on (3.3), as

$$\lambda_{rr} = \frac{1}{4}\sqrt{\frac{\sigma}{\rho_l a_c}} = \frac{1}{4}\sqrt{Rh}, \tag{C3}$$

where the coefficient $1/4$ is used to match their scaling law to their data. Again, this coefficient is included implicitly in their plots but is not mentioned explicitly in their work. Note that the standard coefficient for λ_{RT} (equation (3.3)) is ≈ 11. The acceleration vector in this case is normal to the outer surface of the cap such that the nodes of the receding rim are ejected outwards, which matches the present case of the breakup of bags in droplet aerodynamic breakup. In the present case, where the bag does not have a uniform thickness, the rim experiences an additional acceleration due to its slowing as a result of

the increasing bag thickness near the rim; however, this recession acceleration, a_{rec}, is much smaller than the centripetal acceleration in the present experiments, as shown in figure 34(*b*); thus, the centripetal acceleration is dominant, and the recession acceleration can be ignored.

A final view of the dynamics of the recession in both planar sheets and surface bubbles is provided by Wang *et al.* (2018). In this theory, the thickness of the receding rim, b, is given, universally, by the criterion $Bo = \rho_l b^2 a/\sigma = 1$, where the acceleration used for the case of the surface bubble (i.e. the spherical cap) is taken as the centripetal acceleration, given by (4.2). The receding rim thickness is thus found by rearranging $Bo = 1$, giving (4.3). The receding rim, of thickness b, is then unstable to the Rayleigh–Plateau instability (equation (3.5)).

The above four theories are compared with the present experiments in figure 35. The markers in the figure indicate the values attained by the theories when the maximal acceleration is achieved (h_{min} and $u_{rr,max}$), while the bars denote the variation achieved when the minimal acceleration is used (h_{max} and $u_{rr,min}$). Note that in figure 35, the calculations are based on experimental measurements of u_{rr} (which is used with (4.1) to find h) and R.

Comparing the four theories presented above in figure 35, the theory that best matches the present data for the recession of bags in aerodynamic droplet breakup is that of Wang *et al.* (2018), where most of the data, given the highest acceleration at h_{min} and $u_{rr,max}$, lie within the predicted range of $\lambda \to 2\lambda$.

REFERENCES

ANSYS INC 2011 *ANSYS FLUENT User's Guide Release 14.0*. Canonsburg, PA.

ASHGRIZ, N. 2011 *Handbook of Atomization and Sprays: Theory and Applications*. Springer.

BEHZAD, M., ASHGRIZ, N. & KARNEY, B.W. 2016 Surface breakup of a non-turbulent liquid jet injected into a high pressure gaseous crossflow. *Intl J. Multiphase Flow* **80**, 100–117.

BOSTWICK, J.B. & STEEN, P.H. 2010 Stability of constrained cylindrical interfaces and the torus lift of Plateau-Rayleigh. *J. Fluid Mech.* **647**, 201–219.

BOUROUIBA, L. 2021 The fluid dynamics of disease transmission. *Annu. Rev. Fluid Mech.* **53**, 473–508.

CHANDRASEKHAR, S. 1961 *Hydrodynamic and Hydromagnetic Stability*. Dover Publications, Inc.

CHOU, W.-H. & FAETH, G. 1998 Temporal properties of secondary drop breakup in the bag breakup regime. *Intl. J. Multiphase Flow* **24** (6), 889–912.

CULICK, F.E.C. 1960 Comments on a ruptured soap film. *J. Appl. Phys.* **31** (6), 1128–1129.

DAI, Z. & FAETH, G.M. 2001 Temporal properties of secondary drop breakup in the multimode breakup regime. *Intl J. Multiphase Flow* **27**, 217–236.

FLOCK, A.K., GUILDENBECHER, D.R., CHEN, J., SOJKA, P.E. & BAUER, H.-J. 2012 Experimental statistics of droplet trajectory and air flow during aerodynamic fragmentation of liquid drops. *Intl J. Multiphase Flow* **47**, 37–49.

GRANT, R.P. & MIDDLEMAN, S. 1966 Newtonian jet stability. *AIChE J.* **12** (4), 669–678.

GUILDENBECHER, D.R., GAO, J., CHEN, J. & SOJKA, P.E. 2017 Characterization of drop aerodynamic fragmentation in the bag and sheet-thinning regimes by crossed-beam, two-view, digital in-line holography. *Intl J. Multiphase Flow* **94**, 107–122.

GUILDENBECHER, D.R., LÓPEZ-RIVERA, C. & SOJKA, P.E. 2009 Secondary atomization. *Exp. Fluids* **46** (3), 371–402.

HAN, J. & TRYGGVASON, G. 2001 Secondary breakup of a axisymmetric liquid drops. II. Impulsive acceleration. *Phys. Fluids* **13** (6), 1554–1565.

HSIANG, L.P. & FAETH, G.M. 1992 Near-limit drop deformation and secondary breakup. *Intl J. Multiphase Flow* **18** (5), 635–652.

JACKIW, I.M. & ASHGRIZ, N. 2021 On aerodynamic droplet breakup. *J. Fluid Mech.* **913**, A33.

JAIN, S.S., TYAGI, N., PRAKASH, R.S., RAVIKRISHNA, R.V. & TOMAR, G. 2019 Secondary breakup of drops at moderate Weber numbers: effect of density ratio and Reynolds number. *Intl J. Multiphase Flow* **117**, 25–41. arXiv: 1803.02989.

JALAAL, M. & MEHRAVARAN, K. 2014 Transient growth of droplet instabilities in a stream. *Phys. Fluids* **26**, 012101.

JARRAHBASHI, D., SIRIGNANO, W.A., POPOV, P.P. & HUSSAIN, F. 2016 Early spray development at high gas density: hole, ligament and bridge formations. *J. Fluid Mech.* **792**, 186–231.

JOSEPH, D.D., BEAVERS, G.S. & FUNADA, T. 2002 Rayleigh–Taylor instability of viscoelastic drops at high weber numbers. *J. Fluid Mech.* **453**, 109–132.

KESHAVARZ, B., HOUZE, E.C., MOORE, J.R., KOERNER, M.R. & MCKINLEY, G.H. 2020 Rotary atomization of newtonian and viscoelastic liquids. *Phys. Rev. Fluids* **5** (3), 033601.

KRECHETNIKOV, R. 2010 Stability of liquid sheet edges. *Phys. Fluids* **22** (9), 092101.

LHUISSIER, H. & VILLERMAUX, E. 2009 Soap films burst like flapping flags. *Phys. Rev. Lett.* **103** (5), 054501.

LHUISSIER, H. & VILLERMAUX, E. 2011 The destabilization of an initially thick liquid sheet edge. *Phys. Fluids* **23** (9), 091705.

LHUISSIER, H. & VILLERMAUX, E. 2012 Bursting bubble aerosols. *J. Fluid Mech.* **696**, 5–44.

MARCOTTE, F. & ZALESKI, S. 2019 Density contrast matters for drop fragmentation thresholds at low Ohnesorge number. *Phys. Rev. Fluids* **4** (10), 1–16. arXiv:1907.10711.

MARMOTTANT, P.H. & VILLERMAUX, E. 2004 On spray formation. *J. Fluid Mech.* **498** (498), 73–111.

MEHRABIAN, H. & FENG, J.J. 2013 Capillary breakup of a liquid torus. *J. Fluid Mech.* **717**, 281–292.

NÉEL, B., LHUISSIER, H. & VILLERMAUX, E. 2020 'Fines' from the collision of liquid rims. *J. Fluid Mech.* **893**, A16.

OBENAUF, D.G. & SOJKA, P.E. 2021 Theoretical deformation modeling and drop size prediction in the multimode breakup regime theoretical deformation modeling and drop size prediction in the multimode breakup regime. *Phys. Fluids* **33**, 092113.

OPFER, L., ROISMAN, I.V., VENZMER, J., KLOSTERMANN, M. & TROPEA, C. 2014 Droplet-air collision dynamics: evolution of the film thickness. *Phys. Rev.* E **89** (1), 013023.

O'ROURKE, P.J. & AMSDEN, A.A. 1987 The tab method for numerical calculation of spray droplet breakup. *SAE Tech. Paper Series* 872089.

PILCH, M. & ERDMAN, C.A. 1987 Use of breakup time data and velocity history data to predict the maximum size of stable fragments for acceleration-induced breakup of a liquid drop. *Intl J. Multiphase Flow* **13** (6), 741–757.

POULAIN, S., VILLERMAUX, E. & BOUROUIBA, L. 2018 Ageing and burst of surface bubbles. *J. Fluid Mech.* **851**, 636–671.

QIAN, L., ZHONG, X., ZHU, C. & LIN, J. 2021 An experimental investigation on the secondary breakup of carboxymethyl cellulose droplets. *Intl J. Multiphase Flow* **136**, 103526.

RANGER, A.A. & NICOLLS, J.A. 1969 Aerodynamic shattering of liquid drops. *AIAA J.* **7** (2), 285–290.

RAYLEIGH, LORD 1878 On the instability of jets. *Phil. Mag.* **36**, 4–13.

RIMBERT, N., CASTRILLON ESCOBAR, S., MEIGNEN, R., HADJ-ACHOUR, M. & GRADECK, M. 2020 Spheroidal droplet deformation, oscillation and breakup in uniform outer flow. *J. Fluid Mech.* **904**, A15.

SAVTCHENKO, S. & ASHGRIZ, N. 2005 Temporal instability of a capillary jet with a source of mass. *Phys. Fluids* **17** (11), 112102.

SHARMA, S., SINGH, A.P., RAO, S.S., KUMAR, A. & BASU, S. 2021 Shock induced aerobreakup of a droplet. *J. Fluid Mech.* **929**, A27.

STROTOS, G., MALGARINOS, I., NIKOLOPOULOS, N. & GAVAISES, M. 2016 Predicting droplet deformation and breakup for moderate Weber numbers. *Intl J. Multiphase Flow* **85**, 96–109.

THEOFANOUS, G.T. & LI, J.G. 2008 On the physics of aerobreakup. *Phys. Fluids* **20** (5), 052103.

THEOFANOUS, T.G., LI, G.J. & DINH, T.N. 2004 Aerobreakup in rarefied supersonic gas flows. *J. Fluids Engng* **126** (4), 516–527.

VILLERMAUX, E. 2020 Fragmentation versus cohesion. *J. Fluid Mech.* **898**, P1.

VILLERMAUX, E. & BOSSA, B. 2009 Single-drop fragmentation determines size distribution of raindrops. *Nat. Phys.* **5** (9), 697–702.

VILLERMAUX, E., MARMOTTANT, P. & DUPLAT, J. 2004 Ligament-mediated spray formation. *Phys. Rev. Lett.* **92** (7), 074501.

VILLERMAUX, E., PISTRE, V. & LHUISSIER, H. 2013 The viscous savart sheet. *J. Fluid Mech.* **730**, 607–625.

VLEDOUTS, A., QUINARD, J., VANDENBERGHE, N. & VILLERMAUX, E. 2016 Explosive fragmentation of liquid shells. *J. Fluid Mech.* **788**, 246–273.

WANG, Y. & BOUROUIBA, L. 2021 Growth and breakup of ligaments in unsteady fragmentation. *J. Fluid Mech.* **910**, A39.

WANG, Y., DANDEKAR, R., BUSTOS, N., POULAIN, S. & BOUROUIBA, L. 2018 Universal rim thickness in unsteady sheet fragmentation. *Phys. Rev. Lett.* **120** (20), 204503.

XIAO, F., DIANAT, M. & MCGUIRK, J.J. 2016 A robust interface method for drop formation and breakup simulation at high density ratio using an extrapolated liquid velocity. *Comput. Fluids* **136**, 402–420.

XU, Z., WANG, T. & CHE, Z. 2020 Droplet deformation and breakup in shear flow of air. *Phys. Fluids* **32** (5), 052109.

ZANDIAN, A., SIRIGNANO, W.A. & HUSSAIN, F. 2019 Vorticity dynamics in a spatially developing liquid jet inside a co-flowing gas. *J. Fluid Mech.* **877**, 429–470.

ZHAO, H., LIU, H.-F., CAO, X.-K., LI, W.-F. & XU, J.-L. 2011 Breakup characteristics of liquid drops in bag regime by a continuous and uniform air jet flow. *Intl J. Multiphase Flow* **37** (5), 530–534.

ZHAO, H., LIU, H.-F., LI, W.-F. & XU, J.-L. 2010 Morphological classification of low viscosity drop bag breakup in a continuous air jet stream. *Phys. Fluids* **22**, 114103.